MNRAS 000, 1–16 (2019) Preprint 23 January 2022 Compiled using MNRAS LATEX style file v3.0

Chemical Abundances Of Open Clusters From High-Resolution Infrared Spectra. II. NGC 752

G. Böcek Topcu[1]★, M. Afşar[1,2], C. Sneden[2], C. A. Pilachowski[3], P. A. Denissenkov[4], D. A. VandenBerg[4], D. Wright[2], G. N. Mace[2], D. T. Jaffe[2], E. Strickland[2], H. Kim[5], and K. R. Sokal[2]

[1]*Department of Astronomy and Space Sciences, Ege University, 35100 Bornova, İzmir, Turkey*
[2]*Department of Astronomy and McDonald Observatory, The University of Texas, Austin, TX 78712*
[3]*Indiana University, Department of Astronomy SW319, 727 E 3rd Street, Bloomington, IN 47405 USA*
[4]*Department of Physics and Astronomy, University of Victoria, Victoria, BC, V8W 2Y2, Canada*
[5]*Gemini Observatory, Casilla 603, La Serena, Chile*

Accepted 2019 October 18

ABSTRACT

We present a detailed near-infrared chemical abundance analysis of 10 red giant members of the Galactic open cluster NGC 752. High-resolution (R≃45000) near-infrared spectral data were gathered with the Immersion Grating Infrared Spectrograph (IGRINS), providing simultaneous coverage of the complete *H* and *K* bands. We derived the abundances of H-burning (C, N, O), α (Mg, Si, S, Ca), light odd-Z (Na, Al, P, K), Fe-group (Sc, Ti, Cr, Fe, Co, Ni) and neutron-capture (Ce, Nd, Yb) elements. We report the abundances of S, P, K, Ce, and Yb in NGC 752 for the first time. Our analysis yields solar metallicity and solar abundance ratios for almost all of the elements heavier than the CNO group in NGC 752. O and N abundances were measured from a number of OH and CN features in the *H* band, and C abundances were determined mainly from CO molecular lines in the *K* band. High excitation C I lines present in both near-infrared and optical spectra were also included in the C abundance determinations. Carbon isotopic ratios were derived from the R-branch band heads of first overtone (2−0) and (3−1) ^{12}CO and (2−0) ^{13}CO lines near 23440 Å and (3−1) ^{13}CO lines at about 23730 Å. The CNO abundances and ^{12}C/^{13}C ratios are all consistent with our giants having completed "first dredge-up" envelope mixing of CN-cyle products. We independently assessed NGC 752 stellar membership from Gaia astrometry, leading to a new color-magnitude diagram for this cluster. Applications of Victoria isochrones and MESA models to these data yield an updated NGC 752 cluster age (1.52 Gyr) and evolutionary stage indications for the program stars. The photometric evidence and spectroscopic light element abundances all suggest that the most, perhaps all of the program stars are members of the helium-burning red clump in this cluster.

Key words: stars: abundances – stars: atmospheres. Galaxy: open clusters and associations: individual: NGC 752

1 INTRODUCTION

Open star clusters provide important snapshots of the chemistry of the Galactic disk with time because they can be photometrically tagged with ages, which are difficult to assess for individual field stars. Most open clusters (OCs) are young, $t \leq 2$ Gyr. Very few of them are truly old, $t > 7$ Gyr; only Be 17 and NGC 6791 appear to have ages approaching 10 Gyr (e.g., Salaris et al. 2004, Brogaard et al. 2012). Fortunately there are many intermediate-age clusters close enough to the Sun that chemical compositions of their brighter members can be studied at high spectroscopic resolution. The recent Gaia DR2 catalog now provides opportunities for more accurate membership and evolutionary state data for OC red giant members. Several groups are conducting extensive OC abundance studies using echelle spectrographs in the optical spectral region.

Optical spectroscopy of OCs has a fundamental observational

★ Contact e-mail: gamzebocek@gmail.com (GBT); melike.afsar@ege.edu.tr (MA); chris@verdi.as.utexas.edu (CS); cpilacho@indiana.edu (CAP); pavelden@uvic.ca (PAD); vandenbe@uvic.ca (DAV); gmace@astro.as.utexas.edu (GNM); hkim@gemini.edu (HK); ksokal@utexas.edu (KS); dtj@astro.as.utexas.edu (DTJ)

limit caused by Galactic disk dust extinction. While more than 1000 OCs have been cataloged, most are too obscured to yield detailed information at optical wavelengths. This problem is especially acute for clusters at small Galactocentric radii. High-resolution spectroscopy at more transparent infrared wavelengths (IR, $\lambda \geq 1$ μm) is essential for further progress in OC chemical composition studies.

We have begun a program to use H and K band high-resolution spectroscopy to determine reliable metallicities and elemental abundance ratios for OCs spanning a large range of Galactocentric distances. Special emphasis is put on determining accurate abundances for the CNO group and other light elements, which have many transitions in these IR bands. As steps toward this goal we first are performing combined optical/infrared spectroscopic analyses of three relatively nearby and well-studied intermediate-age OCs that suffer only small amounts of interstellar dust extinction: NGC 6940, NGC 752, and M67. Our IR spectra are obtained with the Immersion Grating Infrared Spectrograph (IGRINS), which offers complete H and K spectral coverage (1.45−2.5 μm), with a band gap of only 0.01 μm lost instrumentally between the two bands (the gap due to telluric absorption is ∼0.2 μm). IGRINS delivers high spectral resolution similar to those of most optical spectrographs used for abundance analysis.

For NGC 6940, Böcek Topcu et al. (2019), hereafter Paper 1, reported analyses of IGRINS spectra of 12 red giant members, the same stars with atmospheric parameters and detailed abundance sets derived from high-resolution optical spectra by Böcek Topcu et al. (2016) (hereafter BT16). Among their principal results were: (a) good agreement in all cases of optical and IR abundances; (b) determination for the first time in NGC 6940 the abundances of S, P, K, Ce, and Yb, and much strengthened abundances of Mg, Al, Si, and Ca; (c) derivation of much more reliable abundances of the CNO group; (d) discovery of one star with evidence of high-temperature proton fusion products; and (e) improved assessment of the NGC 6940 color-magnitude diagram, with clear assignment of most of the program stars to the He-burning red clump.

In this paper we report results of a similar optical/IR study for 10 red giant (RG) members of NGC 752. This relatively nearby OC has been the subject of several abundance studies (e.g., Pilachowski & Hobbs 1988; Carrera & Pancino 2011; Reddy et al. 2012). Recently Lum & Boesgaard (2019) have presented an extensive large-sample analysis of 6 giant and 23 main-sequence stars. Our optical spectroscopic investigation was published in Böcek Topcu et al. (2015) (hereafter BT15). In this study we focus especially on the CNO abundances and $^{12}C/^{13}C$ ratios, interpreting the results within a more complete wavelength window. This larger spectral coverage leads us to a better analysis of the evolutionary status of the RG members. In addition to the red giant abundances derived from IGRINS spectra, we have revisited the questions of the distance and age of NGC 752 with *Gaia* DR2 data, and have re-considered the evolutionary states of these stars via new stellar isochrone computations. The Gaia kinematic and photometric data leading to NGC 752 membership, distance, and age are discussed in §2. In §3 we summarize the IGRINS observations and reductions. The methods used to derive the chemical abundances and the temperatures of the target stars are described in §4 and §5, respectively, while the results of the abundance determinations are given in section §6. The fitting of isochrones to the CMD of NGC 752, resulting in our best estimate of the cluster age, is discussed in §7. We compare stellar model predictions to the observed cluster RC stars in §8, and summarize the main results of this investigation in §9.

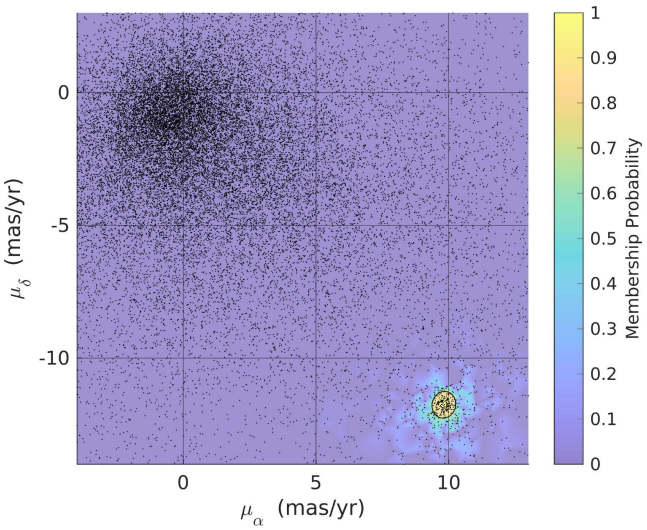

Figure 1. Vector point diagram of our data set, where each dot shows the proper motion components of a star in right ascension (μ_α) and declination (μ_δ). The 95% confidence ellipse in the lower right corner encircles most of the cluster stars and represents the intrinsic cluster center and dispersion. The colors, defined in the side bar, signify NGC 752 membership probabilities for each star. The total data set consisted of more stars more widely separated in proper motion from the field and cluster groups; they have been omitted for clarity in this plot.

2 MEMBERSHIP ASSIGNMENT USING *GAIA* DR2

For determination of our NGC 752 member set, we created a Gaussian mixture model. This model was built using proper motion data from the *Gaia* (Gaia Collaboration et al. 2016) Data Release 2 (Gaia Collaboration et al. 2018). All stars that had *Gaia* DR2 proper motions and resided within 75′ of the approximate NGC 752 cluster center, $\alpha_{2000} = 1^h57^m41.0^s$ and $\delta_{2000} = +37°47'6''$, were considered for membership. A vector point diagram for these stars is shown in Figure 1. Each dot represents the proper motion components of a single candidate star.

Fitting mixture models is an applied statistical method that allows for the Bayesian determination of membership probabilities for individual stars. Open cluster applications of membership models like ours date at least back to Sanders (1971), whose model is fundamentally similar to ours: the sum of two normal probability densities – bivariate in the case of proper motion data – is fit to observed right ascension and declination proper motion components. Our probability density function is of the form

$$\Phi(\mu_{x_i}, \mu_{y_i}, \epsilon_{x_i}, \epsilon_{y_i}) = \phi_c + \phi_f, \quad (1)$$

where μ_{x_i} and μ_{y_i} are the proper motion components for the i^{th} star in our data set, and ϵ_{x_i} and ϵ_{y_i} are their respective errors.

ϕ_c and ϕ_f are Gaussians and represent the cluster and field star distributions, respectively. Both Gaussians are symmetrical and elliptical. It is common to make the assumption of a circular cluster distribution, but we have left it as elliptical for increased accuracy. In addition, we have adopted a method derived by Zhao & He (1990) that takes into account not only the intrinsic dispersions of ϕ_c and ϕ_f but also the observed *Gaia* DR2 errors for each individual star. In total, there are 11 parameters needed to characterize the distributions ϕ_c and ϕ_f in our model. After we solved for these, cluster membership probabilities were calculated. Figure 1 presents the final probabilities for stars within the proper motion ranges

Table 1. Kinematics and radial velocities.

Star	Gaia DR2 identifications	$\pi_{(Gaia)}$ (mas yr^{-1})	$\mu_{\alpha\ (Gaia)}$ (mas yr^{-1})	$\mu_{\delta\ (Gaia)}$ (mas yr^{-1})	RV[a] (km s^{-1})	RV$_{(\text{Paper 1})}$ (km s^{-1})	RV$_{(Gaia)}$ (km s^{-1})
MMU 1	342554191959774720	2.081 ± 0.049	9.780 ± 0.082	−12.003 ± 0.090	5.34 ± 0.24	4.73 ± 0.20	5.29 ± 0.35
MMU 3	342554187663431424	2.101 ± 0.047	9.670 ± 0.078	−11.821 ± 0.082	4.69 ± 0.29	4.11 ± 0.20	5.38 ± 0.20
MMU 11	343118619382072832	2.251 ± 0.066	9.811 ± 0.094	−12.244 ± 0.099	5.08 ± 0.26	4.45 ± 0.19	5.63 ± 0.11
MMU 24	342929297223676160	2.158 ± 0.049	9.602 ± 0.102	−11.940 ± 0.094	4.79 ± 0.18	4.86 ± 0.19	5.70 ± 0.23
MMU 27	342536702852966784	2.174 ± 0.049	9.620 ± 0.084	−11.701 ± 0.097	4.06 ± 0.18	4.39 ± 0.19	4.93 ± 0.18
MMU 77	342532923281905408	2.205 ± 0.050	9.827 ± 0.077	−11.905 ± 0.080	4.89 ± 0.24	4.58 ± 0.20	4.83 ± 1.23
MMU 137	342937195667536512	2.149 ± 0.042	9.535 ± 0.085	−11.883 ± 0.082	5.17 ± 0.24	5.59 ± 0.20	5.60 ± 0.18
MMU 295	342893803614055168	2.201 ± 0.046	9.404 ± 0.104	−11.593 ± 0.087	5.29 ± 0.27	6.32 ± 0.23	
MMU 311	342890127122193280	2.229 ± 0.056	9.701 ± 0.112	−11.331 ± 0.106	5.69 ± 0.24	5.19 ± 0.19	5.67 ± 0.12
MMU 1367	342899537393760512	2.251 ± 0.052	9.688 ± 0.094	−11.794 ± 0.106	4.69 ± 0.24	3.98 ± 0.19	5.09 ± 0.23
RV (cluster mean)					4.97 ± 0.24	4.82 ± 0.20	5.35 ± 0.31

[a] This study.

Table 2. Basic parameters of the program stars and summary of IGRINS observations.

Star	RA[a] (2000)	DEC[a] (2000)	V[b]	H[c]	K[c]	G[a]	$(G_{BP} - G_{RP})^{d}$	$(B-V)_0$	$(V-K)_0$	Date (UT)	S/N (s)
MMU 1	01 55 12.62	37 50 14.55	9.50	7.37	7.23	9.23	1.13	0.92	2.17	02 12 2015	108
MMU 3	01 55 15.29	37 50 31.30	9.57	7.32	7.20	9.28	1.16	0.96	2.27	02 12 2015	106
MMU 11	01 55 27.67	37 59 55.24	9.29	7.16	7.04	9.03	1.12	0.93	2.15	02 12 2015	120
MMU 24	01 55 39.37	37 52 52.51	8.92	6.67	6.55	8.65	1.16	0.98	2.28	03 12 2015	109
MMU 27	01 55 42.39	37 37 54.57	9.16	6.90	6.80	8.88	1.17	0.98	2.27	03 12 2015	117
MMU 77	01 56 21.64	37 36 08.43	9.38	7.05	6.92	9.09	1.21	0.99	2.36	03 12 2015	117
MMU 137	01 57 03.11	38 08 02.65	8.93	6.66	6.54	8.64	1.18	0.99	2.29	04 12 2015	119
MMU 295	01 58 29.82	37 51 37.57	9.30	7.17	7.04	9.05	1.13	0.93	2.17	04 12 2015	141
MMU 311	01 58 52.90	37 48 57.23	9.06	6.80	6.64	8.77	1.20	1.00	2.33	04 12 2015	113
MMU 1367	01 59 14.80	38 00 55.29	9.01	6.77	6.65	8.72	1.18	0.98	2.26	26 11 2018	113

[a] Gaia Collaboration et al. (2018)
[b] Daniel et al. (1994)
[c] Cutri et al. (2003)
[d] Cantat-Gaudin et al. (2018)

plotted. See the appendix for more detail on the exact forms of ϕ_c and ϕ_f and the techniques used to solve for the parameters.

In a mixture model such as ours, it is inevitable that some field stars will pass the cluster membership probability cutoff simply due to random chance. To mitigate this effect, we imposed parallax bounds on the remaining stars. By examination of the parallax density of the stars remaining after the proper motion cutoff, we found that the parallax distribution for NGC 752 peaked at ≃2.235 mas with a base width of ≃0.8 mas. We therefore set parallax bounds of 1.735 mas to 2.735 mas. All stars that passed a 50% proper motion model cutoff and fell within these parallax bounds were considered to be physical cluster members.

Our membership study was performed independently of any other NGC 752 membership analysis. Our computations yield cluster parameters of μ_α = 9.827±0.017 mas/yr, μ_δ = −11.782±0.019 mas/yr, and parallax p= 2.229±0.009 mas. This corresponds to a distance of 448 pc and a true distance modulus $(m - M)_0$ = 8.26, which has been adopted in the fitting of isochrones to the observed CMD in §7. We caution the reader that our parallax uncertainty for NGC 752 is purely statistical; a more realistic estimate would take into account possible systematic *Gaia* uncertainties, which Arenou et al. (2018) suggest can be as large as 0.03 mas. Recently Cantat-Gaudin et al. (2018) have performed a membership study of NGC 752 using very different methods. They suggest cluster parameters μ_α = 9.810±0.019 mas/yr, μ_δ = −11.713±0.019 mas/yr, and p = 2.239±0.005 mas. Although our study focused on proper motions and we do not claim to have determined precise parallax estimates, our results are essentially in agreement with their work.

In Table 1 we have listed the program stars with their *Gaia* DR2 identifications, parallaxes and proper motions. Table 1 also contains radial velocities (RVs) from *Gaia* (Gaia Collaboration et al. 2018), optical (BT15) and *IR* spectra. The *IR* RVs were measured applying a similar method described in Paper 1 using at least 10 spectral orders that are less affected by the atmospheric telluric lines. The mean cluster RVs from these measurements agree well within the mutual uncertainties: $\langle RV\rangle_{\rm opt}$ = 4.82 ± 0.20 kms^{-1} (σ = 0.71), $\langle RV\rangle_{\rm IR}$ = 4.97±0.24 kms^{-1} (σ = 0.45), and $\langle RV\rangle_{\rm Gaia}$ = 5.35±0.31 kms^{-1} (σ = 0.33) (from 9 RGs).

3 OBSERVATIONS AND DATA REDUCTION

We gathered IGRINS H- and K-band high resolution spectra for the 10 NGC 752 RG members studied in the optical spectral region by BT15. The stars chosen for that paper were selected from the radial velocity membership catalog of Mermilliod et al. (2008), before the release of Gaia DR2 astrometric data. The membership analysis

Table 3. Model atmosphere parameters and [Fe/H] abundances from both wavelength regions.

Star	$T_{\rm eff}$ (K)	$T_{\rm eff\,(Gaia)}$ (K)	$T_{\rm eff\,(LDR)}$ (K)	log g	ξ_t (km s^{-1})	[Fe I/H] (opt)	σ (opt)	# (opt)	[Fe II/H] (opt)	σ (opt)	# (opt)	[Fe I/H] (IR)	σ (IR)	# (IR)
MMU 1	5005	4929	5075	2.95	1.07	0.04	0.07	58	−0.02	0.03	12	0.00	0.06	17
MMU 3	4886	4953	5010	2.76	1.10	−0.05	0.07	62	−0.07	0.06	10	-0.03	0.05	20
MMU 11	4988	4956	5045	2.80	1.14	0.03	0.07	59	−0.01	0.04	11	-0.01	0.06	21
MMU 24	4839	4914	4986	2.42	1.23	−0.05	0.07	57	−0.11	0.04	12	-0.05	0.05	20
MMU 27	4966	4878	4948	2.73	1.16	0.08	0.07	57	−0.06	0.03	11	0.06	0.05	20
MMU 77	4874	4850	4944	2.80	1.15	0.04	0.08	62	−0.06	0.06	11	0.03	0.04	19
MMU 137	4832	4850	4970	2.51	1.29	−0.08	0.06	58	−0.16	0.05	9	-0.09	0.04	19
MMU 295	5039	5050	5053	2.88	1.10	0.07	0.06	58	−0.01	0.04	10	0.03	0.06	20
MMU 311	4874	4846	4959	2.68	1.24	0.07	0.09	62	0.01	0.06	10	0.05	0.06	21
MMU 1367	4831	4831	4985	2.42	1.22	−0.02	0.07	59	−0.08	0.03	12	-0.02	0.08	19

presented here confirms that our targets belong to NGC 752. Additionally, several stars not included here appear to be RG members (this study and B. Twarog, private communication). Future spectroscopic study of these stars would be welcome. The log of the IGRINS observations is given in Table 2 along with the basic parameters of program stars. These stars are all red giants with similar parameters, as indicated by spectroscopic analyses ($T_{\rm eff} \sim 4900$ K, log $g \sim 2.7$; BT15) and by photometric data ($V \simeq 9.2$, $M_V \simeq 1.0$, $(B-V)_0 \simeq 0.97$). Three other stars with similar photometric characteristics satisfy our NGC 752 membership criteria: BD+37 404 (MMU 2054), BD+36 328 (MMU 1533), and BD+37 422 (MMU 110, HD 11811). The derived distance for BD+37 422 is ~30 pc from the cluster mean, but this star is a known spectroscopic binary, so its photometric and astrometric data should be treated with caution. None of these three stars appears to have been subjected to a comprehensive atmospheric and abundance analysis; future spectroscopic studies of them would be of some interest.

Characteristics of the IGRINS instrument have been presented by Yuk et al. (2010) and Park et al. (2014). This spectrograph employs a silicon immersion grating (Gully-Santiago et al. 2012) to achieve resolving power $R \equiv \lambda/\Delta\lambda \simeq 45000$ for the entire H and K bands (1.45 – 2.5 μm) in a single exposure. Almost all of the observations were made with IGRINS installed at the Cassegrain focus of the 2.7m Harlan J. Smith Telescope at McDonald Observatory in 2015 December (Mace et al. 2016). One object, MMU 1367, was observed with IGRINS on Lowell Observatory's 4.3m Discovery Channel Telescope (Mace et al. 2018). Typical exposure times were 300s and used ABBA nod sequences along the spectrograph slit length. We also observed telluric standards with spectral types of B9IV to A0V. They were observed right after each science exposures at very close airmasses to the ones at which program stars were observed. The spectra used in this analysis were reduced using the IGRINS pipeline (Lee et al. 2017). The pipeline performs flat-field correction, A-B frame subtractions to remove skyline emission, wavelength correction using OH emission and telluric absorption, and optimal spectral extraction. Due to their high rotational velocities (~150 km s^{-1}), telluric stars come with extremely broadened absorption features that can be easily distinguished from the atmospheric telluric lines. After removing the extremely broadened features from the spectra of telluric standards, we used the *telluric* task of IRAF[1] to remove the contamination of atmospheric absorption lines from the spectra of our program stars.

[1] http://iraf.noao.edu/

4 MODEL ATMOSPHERES AND ABUNDANCES FROM THE OPTICAL REGION

Model atmospheric parameters (Table 3) of the 10 RG members of NGC 752 were previously presented in BT15, along with the abundances for 26 species of 23 elements present in the optical spectral region (see Table 10 in BT15). In this study, we newly report abundances of species S I, K I, and Ce II from those spectra. We present optical sulfur abundances for our targets for the first time in NGC 752 using the S I triplet centered at 6757.17 Å. Takeda et al. (2016) reported non-local thermodynamic equilibrium (non-LTE) corrections for S I, estimated them to be $\lesssim 0.1$ dex for G-K giants for this blended S feature. We have also repeated the analyses for optical Sc II lines, adopting new log gf values from Lawler et al. (2019). Detailed description of the elemental abundance analysis methods in the optical region were provided in BT15, in which we also derived the solar photospheric abundances following the same procedure applied for the program stars, to obtain the differential values of stellar abundances relative to the Sun. Here we used the same method as in Paper 1, adopting the Asplund et al. (2009) solar photospheric abundances for both regions in order to achieve consistency between optical and IR data sets. These slightly revised relative optical abundances are listed in the upper part of Table 4. Mean abundances of the species and their standard deviations are given in columns 12 and 13 of this table. For the [X/Fe] calculations, we took star-by-star species differences using both Fe I and Fe II abundances as appropriate. We will discuss the differences between the NGC 752 and NGC 6940 abundance sets in §6.7.

5 TEMPERATURE DETERMINATION USING IGRINS DATA

Accurate effective temperatures, gravities, and microturbulent velocities are required for abundance analyses. In our OC studies we have adopted traditional line-by-line equivalent width (EW) analyses to derive atmospheric parameters $T_{\rm eff}$, log g, $\xi_{\rm t}$, and [M/H]. For NGC 752 these parameters derived in BT15 are listed in Table 3 and we have used them for all of the abundances reported in this paper. However, for heavily dust-obscured clusters optical parameter determinations will not be possible, and IR-based methods will be needed. Here we explore IR $T_{\rm eff}$ estimates.

Line-depth ratios (LDR) have proven to be good temperature indicators in several studies (e.g. Gray & Johanson 1991; Kovtyukh et al. 2006; Biazzo et al. 2007a,b). The LDR method is based on depth ratios of high-excitation atomic lines (relatively sensitive to

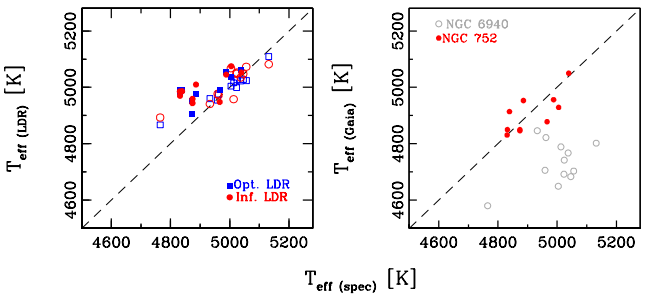

Figure 2. Left panel: comparison of optical and H-band LDR $T_{\rm eff}$ values with those derived spectroscopically in Paper I. Full symbols represents NGC 752 RGs, open symbols are NGC 6940 RGs. Circle's (red) are IR LDR and square symbols (blue) are optical LDR $T_{\rm eff}$ values. Right panel: comparison of *Gaia* temperatures along with the spectroscopic $T_{\rm eff}$'s of the NGC 752 (full red circles) and NGC 6940 (open grey symbols). The dashed line represents equality of the temperatures for both panels.

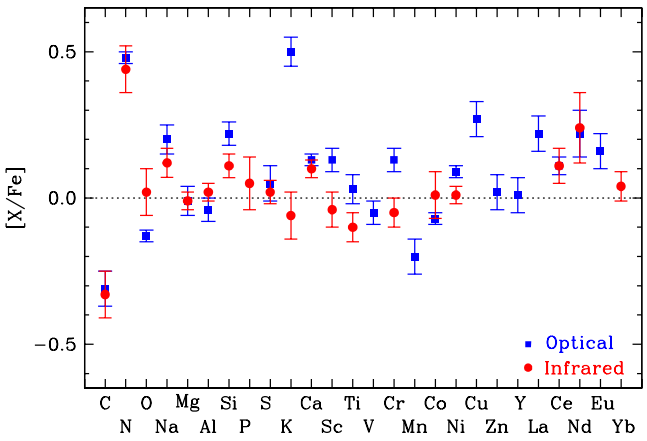

Figure 3. NGC 752 cluster mean elemental abundances from optical (blue symbols) and *IR* (red symbols) spectral region. The data for this figure are from Table 4. For elements represented by two species (Cr and Ti), the average of the species is displayed.

$T_{\rm eff}$) to low-excitation lines (much less sensitive to $T_{\rm eff}$). This spectroscopic method has some attractive features: LDR temperatures are not affected by interstellar reddening and extinction, and they also only weakly depend on other atmospheric parameters for solar metallicity RGs. In our previous optical studies (BT15, BT16), we used the line pairs and equations of Biazzo et al. (2007a,b). Recently, Fukue et al. (2015) have applied the LDR method to the *IR* spectra, and have found nine pairs of absorption lines in the H-band (1.4 – 1.8 μm) to be good $T_{\rm eff}$ indicators. The application of LDR method to the *IR* spectra brings new opportunities, such as access to the most dust obscured stars and the determination of the $T_{\rm eff}$ without any information from the optical region.

We applied the Fukue et al. (2015) relationships to NGC 6940 IGRINS data in Paper 1, and now we have calculated the LDR effective temperatures also for the NGC 752 RGs. $T_{\rm eff}$ results from this LDR method are listed in Table 3 along with other $T_{\rm eff}$ values obtained from the optical region. In Figure 2 (left panel), we compare the temperatures derived from both optical and *IR* LDRs with the spectroscopic temperatures. This comparison indicates that $T_{\rm eff,spec}$ values derived from traditional line-by-line Fe and Ti *EW* analyses and $T_{\rm eff,LDR}$ agree well for $T_{\rm eff} \geq 4900$ K. For cooler RG stars the LDR temperatures become systematically larger. The $T_{\rm eff,LDR}$ of MMU 1367, the coolest ($T_{\rm eff,spec} = 4831$ K) member among others, is 154 K away from its spectroscopic temperature. This star and MMU 311 also deviate similarly in the optical (BT15, Table 6). The *IR*-based LDR temperatures of NGC 6940 shown in the left panel of Figure 2 suggest a similar effect in that cluster also.

The LDR calibration issue is not of importance in our work, as most program stars are warmer than 4900 K, but it should be revisited in the future with larger sets of spectroscopic data in the *IR*. Considering the NGC 752 sample as a whole, on average LDR and spectroscopic temperature are in reasonable accord: $\langle T_{\rm eff,LDR} - T_{\rm eff,spec}\rangle_{\rm IR} = 84 \pm 18$ K, and $\langle T_{\rm eff,LDR} - T_{\rm eff,spec}\rangle_{\rm opt} = 81 \pm 18$ K. Overall the *IR* LDRs provide reliable temperatures in the absence of information from the optical region for giant stars with solar metallicities for the temperature range considered here.

The right panel of Figure 2 shows comparisons of *Gaia* temperatures (Table 3) vs. $T_{\rm eff,spec}$ for the RGs of NGC 752 and NGC 6940. By inspection, *Gaia* and spectroscopic agree well for NGC 752, and for the whole sample $\langle T_{\rm eff,Gaia} - T_{\rm eff,spec.}\rangle_{\rm NGC\ 752} = -8 \pm 17$ K. For NGC 6940 the lack of agreement between spectroscopic and *Gaia* temperatures is clear in Figure 2: $\langle T_{\rm eff,Gaia} - T_{\rm eff,spec.}\rangle_{\rm NGC\ 6940} = -264 \pm 26$ K. *Gaia* temperatures are photometrically based and thus depend on interstellar extinction corrections. For NGC 6940 $E(B-V) = 0.21$, while for NGC 752 the reddening is very small, $E(B-V) = 0.035$. This probably is related to the poor $T_{\rm eff}$ correlation for NGC 6940, but resolution of the question is beyond the scope of this paper.

6 ABUNDANCES FROM THE INFRARED REGION

We determined the abundances of 20 elements in NGC 752 from the IGRINS H and K band spectra. Of these elements, 18 also have optical region abundances reported by BT15. We applied synthetic analyses to all transitions with the same atomic and molecular line lists and methods described in Afşar et al. (2018); see Paper 1 for more detailed discussion. We derived the abundances of H-burning (C, N, O), α (Mg, Si, S, Ca), light odd-Z (Na, Al, P, K), Fe-group (Sc, Ti, Cr, Fe, Co, Ni), and neutron-capture (n-capture) (Ce, Nd, Yb) elements, and also determined ^{12}C/^{13}C ratios. The relative *IR* abundances for our NGC 752 RGs are listed in the second part of Table 4. In Figure 3, we plot the mean *IR* abundances along with the optical ones from BT15, updated as described in §4. The figure shows general agreement between *IR* and optical abundances. Defining $\Delta^{\rm IR}_{\rm opt}$[A/B] = [A/B]$_{\rm IR}$ − [A/B]$_{\rm opt}$, we find $\langle\Delta^{\rm IR}_{\rm opt}$[X/Fe]$\rangle$ = 0.07 ± 0.04 (σ = 0.15) for 18 species with both optical and *IR* abundances. Figure 4 shows optical and *IR* abundances of each species for all program RGs vs. effective temperature. This figure shows that in a small temperature range (∼175 K) that is covered by our RG sample, abundances do not show significant changes with temperature. Both figure 3 and 4 indicate the optical/*IR* agreement for most of the species with a few exceptions: O, Sc, Ti II and K I. The *IR* abundances of these species deviate more than 0.15 dex from their optical counterparts. We will discuss these deviations in the subsections below.

6.1 Fe-group elements:

We have investigated NGC 752 Fe abundances from about 20 Fe I transitions. As noted in our previous studies, there are no known useful Fe II transitions in the IGRINS spectral range. The Fe I

Table 4. Relative abundances and $^{12}C/^{13}C$ ratios of NGC 752 RGs and their cluster means.

Species	MMU												
[X/Fe]	1	3	11	24	27	77	137	295	311	1367	mean	σ	$\#_{max}$
Optical Spectral Region													
Na I	0.20	0.16	0.21	0.27	0.16	0.15	0.30	0.17	0.20	0.23	0.20	0.05	4
Mg I	−0.06	0.03	0.00	0.08	−0.02	−0.02	0.03	−0.09	−0.07	0.00	−0.01	0.05	2
Al I	−0.08	−0.02	−0.08	0.00	−0.08	−0.04	0.02	−0.09	−0.07	−0.03	−0.04	0.04	2
Si I	0.18	0.22	0.20	0.27	0.17	0.22	0.29	0.19	0.22	0.27	0.22	0.04	15
S I*	0.02	0.13	0.04	0.04	−0.01	0.07	0.17	−0.04	0.04	0.06	0.05	0.06	2
K I*	0.47	0.61	0.49	0.54	0.51	0.44	0.47	0.51	0.47	0.52	0.50	0.05	1
Ca I	0.13	0.17	0.12	0.16	0.09	0.13	0.13	0.11	0.12	0.15	0.13	0.02	10
Sc II*	0.08	0.02	0.06	0.06	0.14	0.12	0.09	0.08	0.09	0.03	0.08	0.01	6
Ti I	−0.04	−0.05	−0.08	−0.09	−0.01	−0.01	−0.07	−0.02	−0.06	−0.11	−0.05	0.03	11
Ti II	0.14	0.07	0.10	0.03	0.11	0.04	0.02	0.13	0.02	0.01	0.07	0.05	4
V I	−0.03	−0.04	−0.08	−0.08	−0.02	0.01	−0.06	−0.04	−0.04	−0.11	−0.05	0.04	12
Cr I	0.07	0.10	0.03	0.07	0.07	0.05	0.09	−0.01	−0.01	0.04	0.05	0.04	14
Cr II	0.17	0.17	0.18	0.26	0.20	0.23	0.20	0.25	0.19	0.18	0.20	0.03	3
Mn I	−0.17	−0.23	−0.18	−0.15	−0.24	−0.21	−0.22	−0.30	−0.24	−0.07	−0.20	0.06	3
Co I	−0.07	−0.07	−0.10	−0.08	−0.08	−0.05	−0.06	−0.10	−0.06	−0.09	−0.07	0.02	5
Ni I	0.09	0.07	0.07	0.09	0.10	0.12	0.09	0.12	0.11	0.07	0.09	0.02	29
Cu I	−0.18	−0.31	−0.26	−0.26	−0.27	−0.17	−0.28	−0.37	−0.31	−0.30	−0.27	0.06	1
Zn I	−0.07	0.02	−0.02	0.12	−0.04	0.03	0.09	−0.05	0.05	0.04	0.02	0.06	1
Y II	−0.02	−0.04	0.05	0.08	0.04	0.10	−0.05	0.00	−0.04	−0.06	0.01	0.06	4
La II	0.22	0.17	0.17	0.21	0.25	0.36	0.26	0.20	0.19	0.18	0.22	0.06	4
Ce II*	0.08	0.10	0.07	0.09	0.18	0.14	0.14	0.08	0.10	0.08	0.11	0.03	4
Nd II	0.20	0.04	0.24	0.22	0.33	0.33	0.27	0.19	0.20	0.16	0.22	0.08	3
Eu II	0.11	0.21	0.05	0.21	0.16	0.25	0.21	0.10	0.15	0.14	0.16	0.06	2
log ϵ(Li)	0.15	1.25	1.00	< 0.0	0.95	1.34	< 0.0	< 0.0	0.78	< 0.0			1
$^{12}C/^{13}C$	25	20	25	13	17	25	15	20	15	20	19.5	4.5	CN
C	−0.39	−0.28	−0.27	−0.27	−0.37	−0.39	−0.21	−0.32	−0.37	−0.28	−0.31	0.06	C_2, CH, C I
N	0.51	0.45	0.47	0.50	0.50	0.46	0.48	0.48	0.48	0.47	0.48	0.02	CN
O	−0.15	−0.16	−0.14	−0.14	−0.11	−0.10	−0.10	−0.11	−0.13	−0.14	−0.13	0.02	[O I]
IGRINS H & K Spectral Region													
Na I	0.11	0.02	0.15	0.16	0.10	0.12	0.11	0.11	0.07	0.19	0.12	0.05	5
Mg I	−0.05	−0.01	−0.02	0.01	−0.03	0.03	0.02	−0.05	−0.01	0.02	−0.01	0.03	11
Al I	0.02	−0.05	0.04	0.04	0.01	0.05	0.04	0.04	0.00	0.04	0.02	0.03	6
Si I	0.07	0.10	0.13	0.14	0.10	0.08	0.15	0.10	0.05	0.16	0.11	0.04	11
P I	−0.08	0.16	0.06	0.15	−0.11	0.09	0.09	0.04	0.07	−0.01	0.05	0.09	2
S I	0.02	0.04	0.05	0.03	−0.05	−0.02	0.10	0.02	−0.01	−0.01	0.02	0.04	10
K I	−0.03	0.02	−0.04	−0.07	−0.11	0.00	−0.11	−0.24	−0.08	0.00	−0.06	0.08	2
Ca I	0.12	0.10	0.10	0.11	0.07	0.13	0.10	0.05	0.06	0.14	0.10	0.03	11
Sc I	0.01	−0.11	−0.02	−0.14	−0.10	−0.02	0.01	−0.06	0.04	−0.05	−0.04	0.06	2
Ti I	−0.02	−0.09	−0.05	−0.09	−0.05	0.02	−0.06	−0.10	−0.07	−0.15	−0.06	0.05	10
Ti II	−0.12	−0.08	−0.13	−0.17	−0.16	−0.10	−0.12	−0.16	−0.12	−0.22	−0.14	0.04	1
Cr I	0.00	−0.04	0.00	−0.03	−0.10	−0.10	0.00	−0.13	−0.03	−0.08	−0.05	0.05	3
Co I	−0.01	0.11	−0.11	−0.06	−0.03	0.02	0.07	0.11	0.03	−0.09	0.01	0.08	1
Ni I	0.04	−0.02	0.03	0.03	0.00	0.03	−0.01	−0.03	0.01	−0.02	0.01	0.03	6
Ce II	0.13	0.05	0.13	0.10	0.06	0.20	0.15	0.16	0.13	0.02	0.11	0.06	9
Nd II	0.43	0.15	0.34		0.16	0.19	0.30	0.35	0.21	0.05	0.24	0.12	1
Yb II	0.10	0.04	0.06	0.02	−0.06	0.07	0.04	0.10	0.00	0.00	0.04	0.05	1
$^{12}C/^{13}C$	28	28	28	20	22	30	20	25	23	16	25.0	3.6	CO
C	−0.32	−0.41	−0.31	−0.37	−0.32	−0.30	−0.27	−0.31	−0.31	−0.36	−0.33	0.04	CO, C I
N	0.58	0.48	0.49	0.45	0.41	0.37	0.42	0.48	0.39	0.31	0.44	0.08	CN
O	0.13	0.05	0.01	−0.06	0.06	0.05	−0.04	0.13	0.00	−0.14	0.02	0.08	OH

* This study.

transitions were adopted from Afşar et al. (2018). In Table 3 we list the optical and *IR* Fe abundances for each RG. Optical Fe I and Fe II abundances were derived by using the *EW* method (BT15). The optical cluster means are: $\langle$[Fe I/H]$\rangle_{opt}$ = 0.01 (σ = 0.07) and $\langle$[Fe II/H]$\rangle_{opt}$ = −0.06 (σ = 0.04). The 0.07 dex difference between the neutral and ionized iron abundances stays, in general, within the uncertainty limits. The cluster mean from the *IR* Fe I lines is $\langle$[Fe I/H]$\rangle_{IR}$ = 0.00 (σ = 0.06), clearly in agreement with the optical values within the mutual uncertainties. The metallicity of NGC 752 from the neutral- and ionized-species Fe and Ti lines, $\langle$[M/H]$\rangle$ = −0.07 ± 0.04 (BT15), also agrees well with these values and indicates a solar metallicity for NGC 752.

For other Fe-group elements, we derived abundances from species Sc I, Ti I, Ti II, Cr I, Co I and Ni I. For Sc we used two weak

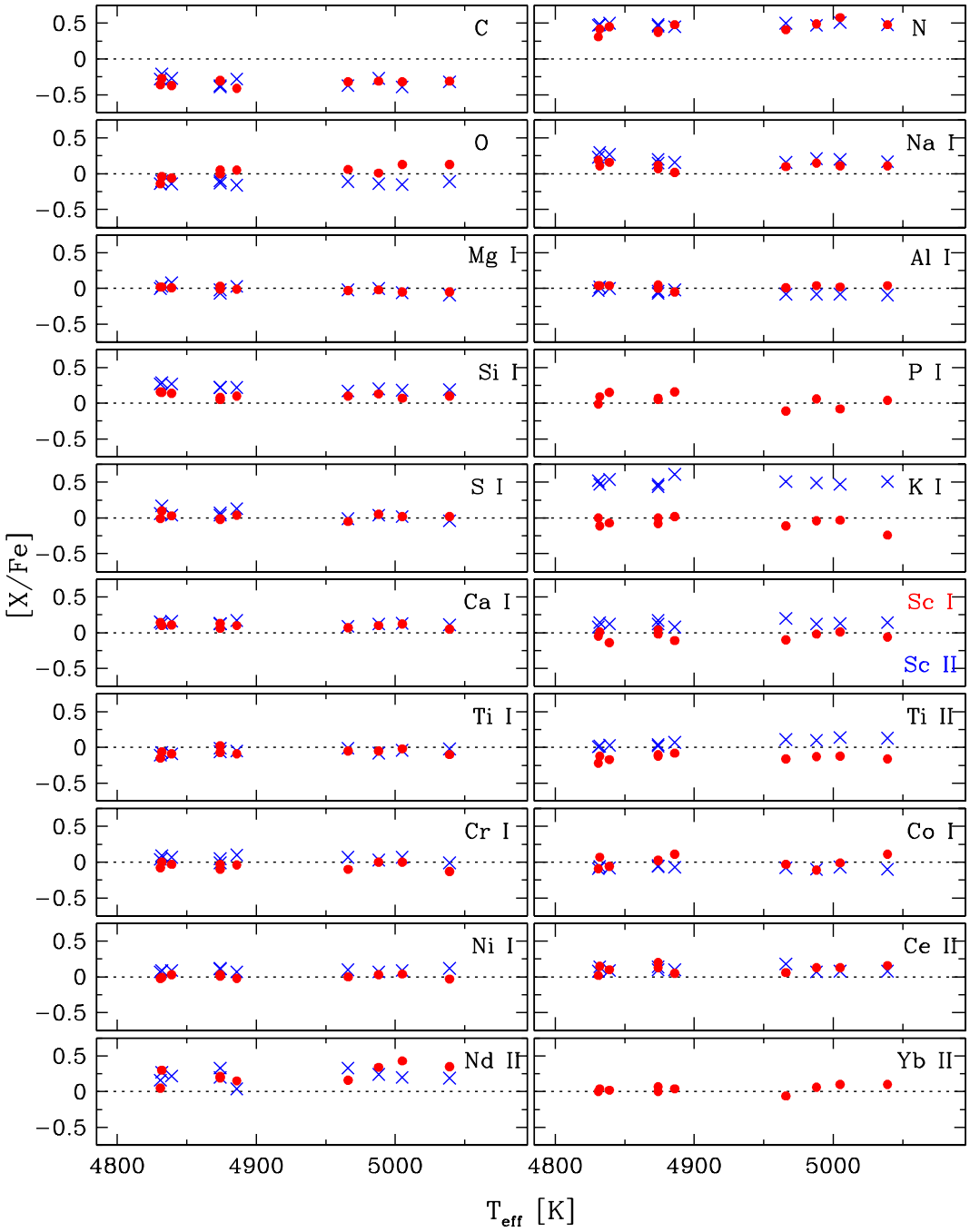

Figure 4. Mean abundances of the species for all NGC 752 program stars plotted as functions of their $T_{\rm eff}$ values. The panels labeled simply C, N, and O are based on multiple abundance indicators that are discussed in §6.5. Optical and *IR* abundances are shown with blue crosses and red dots, respectively. In the Sc panel, Sc I (red dots) and Sc II (blue crosses) represent the measurements from *IR* and optical, respectively.

K band transitions, taking into account their hyperfine structures. We applied synthetic spectrum analysis to these absorption lines and the difference from the optical is $[\rm Sc\,II/Fe]_{opt}$ - $[\rm Sc\,I/Fe]_{IR}$ = 0.12 dex. The difference between two spectral regions resembles the difference between neutral and ionized species of Cr in the optical and Ti both in the optical and *IR*. We calculated Ti abundances from 10 Ti I lines and the one Ti II line at 15783 Å. Although optical and *IR* Ti I abundances are in agreement, for Ti II the difference is $[\rm Ti\,II/Fe]_{opt}$ - $[\rm Ti\,II/Fe]_{IR}$ = 0.20 dex. This situation was also discussed in Paper 1 and Afşar et al. (2018). For 12 RGs of NGC 6940, the difference between the optical and *IR* Ti II abundances was 0.16 dex, and for the three RHB stars presented in Afşar et al. (2018) was also 0.16 dex. The *H*-band Ti II line comes with a CO blend but for the temperature range for our stars its contamination of Ti II feature is negligible. Further investigation of the *IR* Ti II line is needed to better understand the discrepancy between optical and *IR* Ti II abundances. The other Fe-group elements have agreement between optical and IR transitions. The mean [X/Fe] abundance from Table 4 for Fe-group elements is $\langle[\rm X/Fe]\rangle_{\rm IR} = -0.05$ (σ = 0.05) for six

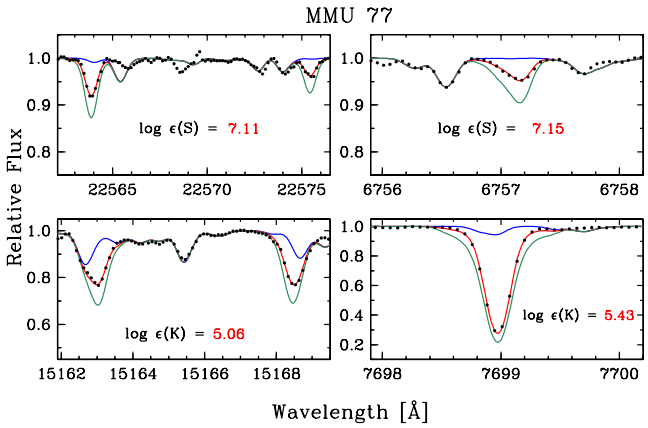

Figure 5. Observed (points) and synthetic spectra (colored lines) of transitions for sulfur and potassium in *IR* and optical wavelengths. In each panel the blue line (in the top) represents a synthesis with no contribution by the element of interest, the red line (in the middle) is for the abundance that best matches the observed spectrum, and the green line (on the bottom) represent the synthesis larger than the best fit by 0.5 dex.

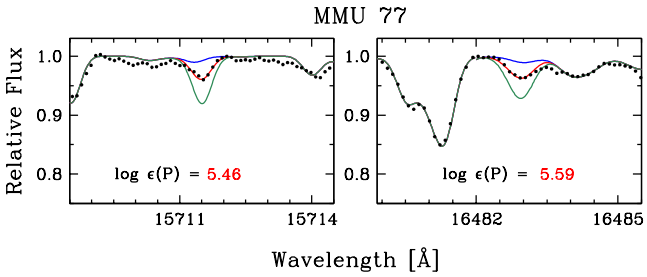

Figure 6. Observed and synthetic spectra of the phosphorus in the *IR*. The symbols and lines have the same meanings as they do in Figure 5.

species and optical mean is $\langle$[X/Fe]$\rangle_{\rm opt} = -0.01$ ($\sigma = 0.14$) for 11 species including V I, Cr II, Mn I, Cu I and Zn I.

6.2 Alpha elements

We derived the abundances of Mg, Si, S and Ca in NGC 752 from their neutral species using the lines in both *H* and *K* bands (Table 4). For the *IR* S I abundance, we made use of about ten transitions in the *H* and *K* bands. In the top panels of Figure 5 observed and synthetic spectra of two S I lines in the *K* band and the combined absorption of three closely-spaced S I lines in the optical domain for MMU 77 are shown. Sulfur abundances are about solar for both optical and *IR* spectral regions; $\langle$[S I/Fe]$\rangle_{\rm opt} = 0.05$ ($\sigma = 0.06$) and $\langle$[S I/Fe]$\rangle_{\rm IR} = 0.02$ ($\sigma = 0.04$). Optical Ca and Si abundances from BT15 have a small line-to-line scatter about 0.03 dex, but Mg, on the other hand, obtained from the spectrum synthesis of two strong Mg lines at 5528 and 5711 Å resulted in ~0.20 dex difference. Mg abundances from the *IR* region were derived from about ten absorption lines with a mean standard deviation of about 0.08 for 10 RGs, which suggests greater reliability for *IR*-based Mg abundances. Mean abundances for α elements $\langle$[α/Fe]$\rangle \equiv \langle$[Mg, Si, S, Ca/Fe]$\rangle$, for both optical and *IR* regions are $\langle$[α/Fe]$\rangle_{\rm opt} = 0.10$ ($\sigma = 0.10$) and $\langle$[α/Fe]$\rangle_{\rm IR} = 0.06$ ($\sigma = 0.06$), which are well in agreement and slightly above solar.

6.3 Odd-Z light elements

The odd-Z light elements investigated in this study are Na, Al and rarely-studied P and K. Their abundances are in Table 4. Na abundances were derived from four neutral *K* band transitions: 22056.4, 22083.7, 23348.4 and 23348.1 Å. To our knowledge, possible non-LTE effects on these transitions have not yet been investigated. The optical and *IR* Na abundances are both above the solar values. The *IR* mean for NGC 752 (Table 4) is $\langle$[Na I/Fe]$\rangle_{\rm IR} = 0.12$ ($\sigma = 0.05$), while the optical mean is $\langle$[Na I/Fe]$\rangle_{\rm opt} = 0.20$ ($\sigma = 0.05$). Al abundances were obtained from two lines in the *H* and four lines in the *K* band. *H* band abundances are always ~0.1 dex lower than the *K* band abundances and the lower *H* band abundances are more in accord with the optical ones: $\langle$[Al I/Fe]$\rangle_{\rm IR} = 0.02$ ($\sigma = 0.03$) and $\langle$[Al I/Fe]$\rangle_{\rm opt} = -0.04$ ($\sigma = 0.04$).

Phosphorus abundances were determined from two weak *H*-band transitions at 15711.5 and 16482.9 Å. As illustrated in Figure 6 for MMU 77, the P I lines always have central depths $\lesssim$5% for the members studied here. The P abundance difference obtained from these two lines is 0.13 dex, but this is an extreme case; for other program stars the agreement is much better, usually <0.1 dex. The mean phosphorus abundance, $\langle$[P I/Fe]$\rangle_{\rm IR} = 0.04$ ($\sigma = 0.09$) is consistent with the solar value.

As noted in §4 we derived NGC 752 optical-region K abundances, using the very strong K I resonance line at 7698.97 Å (lower right panel of Figure 5). Our derived mean K abundance for the cluster is large, $\langle$[K I/Fe]$\rangle_{\rm opt} = 0.50$ ($\sigma = 0.05$), but this resonance line is subject to significant non-LTE effects. Takeda et al. (2002) and Mucciarelli et al. (2017) have computed non-LTE corrections between 0.2 and 0.7 dex for disk/halo stars of various $T_{\rm eff}$−log *g* combinations. Afşar et al. (2018) found ~0.6 dex higher abundances for the 7699 Å line in three RHB stars. Taking into account the non-LTE corrections suggested for 7698.97 Å K I line leads to a conclusion of solar K abundance for our targets. But since this is not based on our own calculations, we have chosen to keep the LTE abundance in Table 4.

Potassium abundances from the *IR* region were derived from two K I lines at 15163.1 and 15168.4 Å which are affected by CN contamination. We illustrate this with observed/synthetic spectrum comparisons in the lower left panel of Figure 5. Unlike the optical resonance line, the *H* band K I lines yield approximately solar abundances: $\langle$[K I/Fe]$\rangle_{\rm IR} = -0.06$ ($\sigma = 0.08$). This consistency suggests that at most very small (or no) non-LTE corrections may be needed for these K lines. Non-LTE studies of all detectable K I lines in cool stars will be welcome.

Following the detailed description of HF analyses in Pilachowski & Pace (2015), we have also inspected the unblended HF feature located at 23358.3 Å in the *K* band region. Unfortunately no obvious absorption of fluorine is detectable in our targets.

6.4 *n*-capture Elements

In this study we have obtained abundances of three *n*-capture elements from their ionized species transitions: Ce and Nd (mostly due to the *s*-process in the solar-system), and Yb (mostly from the *r*-process). Ce abundances were derived from about four transitions, Nd from one weak transition at 16262.04 Å, and Yb also from one weak line at 16498.4 Å. Yb II is blended with CO but that contamination is weak enough to be neglected for the temperature/gravity range for our stars. Mean abundances of all three *n*-capture ele-

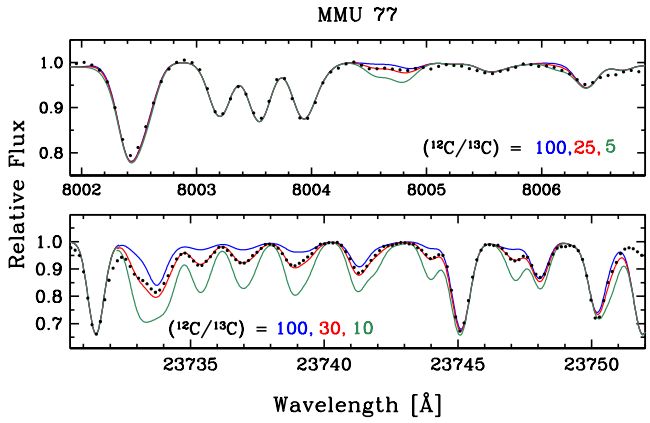

Figure 7. Observed and synthetic spectra illustrating the carbon isotopic ratio of NGC 752 MMU 77 in both optical and *IR* regions. The upper panel is centred on the triplet or ^{13}CN red system (2-0) lines, and the bottom panel shows the ^{13}CO (3-1) R-branch band head region. The blue, red, and green synthesis represent ^{12}C/^{13}C =100, 25, and 5 in the upper panel, and ^{12}C/^{13}C =100, 30, and 10 in the bottom panel, respectively.

ments are about/above solar, $\langle$[Ce II/Fe]$\rangle_{\rm IR}$ = 0.11 (σ = 0.06), $\langle$[Nd II/Fe]$\rangle_{\rm IR}$ = 0.24 (σ = 0.12) and $\langle$[Yb II/Fe]$\rangle_{\rm IR}$ = 0.04 (σ = 0.05) (Table 4). We have also analyzed optical Ce abundances from 5274.23, 5330.56, 5975.82 and 6043.37 Å transitions. The mean value for the NGC 752 RGs is $\langle$[Ce II/Fe]$\rangle_{\rm opt}$ = 0.11 (σ = 0.03), which is in harmony with the *IR* abundance with smaller star-to-star scatter. In BT15 we derived the Nd abundances from two lines at 5255.5 and 5319.8 Å; the overabundance is similar what we found from the *H* band transition, $\langle$[Nd II/Fe]$\rangle_{\rm opt}$ = 0.22 (σ = 0.08). In Paper 1, the RGs of NGC 6940, which were analyzed in the same manner with the NGC 752 RGs in this study, showed slightly over-abundance in *r*-process and more in the *s*-process elements. We observe a similar behavior; the simple mean of the optical and *IR* La, Ce and Nd abundances is $\langle [s-{\rm process/Fe}] \rangle \simeq 0.18$, while mean of Eu and Yb is $\langle [r-{\rm process/Fe}] \rangle \simeq 0.10$.

6.5 The CNO Group

The IGRINS spectral range contains many useful OH, CN and CO molecular bands that can be used to obtain CNO abundances. We have followed the same iterative scheme used in Paper 1 to obtain the CNO abundances. We have also determined carbon abundances from its neutral transitions in both optical and *IR* spectral regions.

There are many OH molecular lines in the *H* band but most of them are very weak for our temperature and metallicity range and also blended with other lines and/or molecular bands. We were able to use about 10 OH molecular lines located between 15200−17700 Å; the abundances for each star in Table 4 are simple means of the abundances derived from individual OH features. The resulting cluster mean is $\langle$[O/Fe]$\rangle_{\rm IR}$ = 0.02 (σ = 0.09) (Table 4). In BT15, we were able use only the [O I] line at 6300.3 Å to determine optical O abundances, and noted that this feature is plagued with Ni I and CN contamination. The calculated mean for the cluster from this line is $\langle$[O/Fe]$\rangle_{\rm opt}$ = −0.13 (σ = 0.02). Having the advantage of obtaining O abundances from many OH features, we rely more on the O abundance we determine from the *IR* region.

Carbon abundances were derived from multiple optical and *IR* species. The summary of the results for each star are given in Table 5. In the *IR*, we used primarily the CO molecular features

Table 5. logϵ Abundances of Carbon in optical and infrared regions.

Star	C I opt	CH opt	C_2 opt	C I *IR*	CO *IR*	mean opt	mean *IR*
MMU 1	8.04	7.90	8.03	8.10	8.11	7.99	8.11
MMU 3	8.16	7.78	7.98	8.00	7.98	7.97	7.99
MMU 11	8.20	7.98	8.08	8.10	8.11	8.08	8.11
MMU 24	8.16	7.80	7.95	8.00	8.02	7.97	8.01
MMU 27	8.14	7.93	8.05	8.13	8.20	8.04	8.17
MMU 77	8.05	7.88	8.05	8.11	8.21	7.99	8.16
MMU 137	8.21	7.83	8.00	8.07	8.07	8.01	8.07
MMU 295	8.18	7.95	8.08	8.11	8.18	8.07	8.15
MMU 311	8.14	7.90	8.04	8.17	8.18	8.03	8.18
MMU 1367	8.18	7.83	8.03	8.06	8.03	8.01	8.05

in the *K* band: ^{12}CO first overtone, Δv = 2, (2-0) and (3-1) bands at 23400 and 23700 Å. The scatter based on different abundance measurements for a single RG is very small, about ∼0.03 dex. The mean C abundance from the CO molecular lines is $\langle$[C/Fe]$\rangle_{\rm CO}$ = −0.32 (σ = 0.06), a value which would be expected after first dredge-up and envelope mixing in metal-rich disk stars. There are second overtone ^{12}CO band heads also in the *H* band but due to relatively high temperatures of our programme stars they are too weak for detection. In BT15 we obtained the carbon abundances from the CH G band, the Swan band heads of C_2 (0-0) at 5155 Å and the (0-1) at 5635 Å (Figure 9 in BT15). These molecular bands are heavily blended with other atomic transitions and the C_2 bands are weak in strength, which makes the spectral analysis challenging in these regions. But from those features BT15 derived $\langle$[C/Fe]$\rangle_{\rm CH,C_2}$ = −0.41 (σ = 0.03). Considering the analytical difficulties for CH and C_2, the ∼0.1 dex difference from the *IR* CO result indicates reasonable accord.

We obtained the carbon abundances also from the high-excitation C I lines. Carbon abundances derived from the C I transitions agree very well with CO results, $\langle$[C I/Fe]$\rangle_{\rm IR}$ = −0.34 (σ = 0.04). As a further check we also determined the C abundances from synthetic spectrum analyses of three high-excitation C I lines located in the optical at 5052.1, 5380.3 and 8335.1 Å. The line-to-line C abundance scatter from these transitions is about 0.1 dex, and the mean abundance for the cluster is $\langle$[C I/Fe]$\rangle_{\rm opt}$ = −0.22 (σ = 0.10), on average only ∼0.14 dex higher compare to the mean C abundance obtained from other features mentioned above.

In Table 5 we have listed the individual and mean carbon abundances. The quoted carbon abundances in this table are the average of the molecular and high-excitation carbon abundances and they are in relatively good agreement; $\langle$[C/Fe]$\rangle_{\rm IR}$ = −0.33 (σ = 0.04), $\langle$[C/Fe]$\rangle_{\rm opt}$ = −0.31 (σ = 0.06).

We obtained nitrogen abundances from the CN molecular transitions in the H-band. We used about 18 CN features between 15000 and 15500 Å, and calculated N abundances. The mean *IR* N abundance is $\langle$[N/Fe]$\rangle_{\rm IR}$ = 0.44 (σ = 0.08). Optical nitrogen abundances were obtained from ^{12}CN and ^{13}CN red system lines in the 7995−8040 Å region in BT15, and the means are in accord with those from the *IR*, $\langle$[N/Fe]$\rangle_{\rm opt}$ = 0.48 (σ = 0.02).

Finally, we measured the ^{12}C/^{13}C ratios from the first overtone ^{12}CO (Δv = 2) (2-0) and (3-1) band lines, which are accompanied by the ^{13}CO band heads near 23440 and 23730 Å. These are more robust features for ^{12}C/^{13}C ratio determination than the standard optical ^{13}CN feature near 8003 Å used by BT15. The top panel of Figure 7 shows that the ^{13}CN triplet, the strongest feature of this band system, is barely detectable in MMU 77 (nor is it much

Table 6. Carbon isotopic ratios of optical and infrared regions.

Stars	^{13}CN (8004 Å)	^{13}CO (23440 Å)	^{13}CO (23730 Å)
MMU 1	25	25	30
MMU 3	25	25	30
MMU 11	25	25	30
MMU 24	13	20	20
MMU 27	17	19	25
MMU 77	25	30	30
MMU 137	15	20	20
MMU 295	20	25	25
MMU 311	15	23	22
MMU 1367	17	15	16

stronger in any NGC 752 star). In contrast, the ^{13}CO features shown in the bottom panel of this figure are much stronger. We compare the optical and *IR* ^{12}C/^{13}C values in Table 6. They are in reasonable accord, given the extreme weakness of the CN bands.

6.6 Abundance Uncertainties

Detailed investigation of the internal and external uncertainty levels of the atmospheric parameters and their effects on the elemental abundances were provided in BT15, in which we calculated an average uncertainty limit of about 150 K by comparing the spectroscopically derived $T_{\rm eff}$ values with the literature, photometric and LDR temperatures. In Table 8 of BT15 we list the sensitivity of derived abundances to the model atmosphere changes within uncertainty limits for the star MMU 77. Additional investigation of LDR temperatures from the *IR* data has shown that our temperature uncertainty limit has remained almost the same as determined in BT15, considering the highest LDR and spectral temperature difference of 154 K for MMU 1367 (see §5). Therefore, in Table 7, we present the sensitivity of derived abundances in the elements only newly studied in this work adopting the same atmospheric parameter uncertainties in BT15. The uncertainties were determined using the *IR* spectra of same star, MMU 77, as applied in BT15. In general, abundance changes are mostly well within 1σ level of the [X/Fe] values (Table 4). However, the sensitivity level of Sc I abundance to the change in temperature stands out. The temperature sensitivity of some *IR* Sc lines has been previously noticed by Thorsbro et al. (2018), based on Sc I lines identified in *K* band of cool M giants observed with NIRSPEC/Keck II. They reported up to 0.2 dex uncertainties in Sc abundances mostly originated from the temperature sensitivity for stars $T_{\rm eff}$ < 3800 K. Although our stars have higher temperatures and the Sc I lines we used are different than those that Thorsbro et al. discussed, caution should be taken in interpreting the *IR* Sc abundances for our stars until the underlying physical process for the temperature sensitivity of Sc lines are better understood.

6.7 Comparison with NGC 6940

We have now derived metallicities and relative abundance ratios for OCs NGC 6940 and NGC 752 with high resolution spectra in the optical spectral region (BT15, BT16) and infrared (BT19, this study). The NGC 6940 optical data were obtained with the Hobby-Eberly Telescope and its high-resolution echelle spectrometer (Tull 1998), and those for NGC 752 with the 2.7m Smith Telescope and Tull echelle spectrometer (Tull et al. 1995); both data sets have high

Table 7. Sensitivity of elemental abundances to the model atmosphere parameter uncertainties for MMU 77.

Species	$\Delta T_{\rm eff}$ (K) −150 / +150	$\Delta\log g$ −0.25 / +0.25	$\Delta\xi_t$ (km s^{-1}) −0.3 / +0.3
P I	0.01 / 0.01	0.09 / −0.09	0.01 / 0.00
S I	−0.06 / 0.09	0.09 / −0.05	−0.03 / 0.03
K I	0.10 / −0.11	0.02 / −0.01	−0.01 / 0.05
Sc I	0.18 / −0.18	0.01 / 0.01	0.01 / 0.00
Ce II	0.08 / −0.06	0.12 / −0.11	−0.03 / 0.03
Yb II	0.05 / −0.05	0.10 / −0.10	−0.02 / 0.03

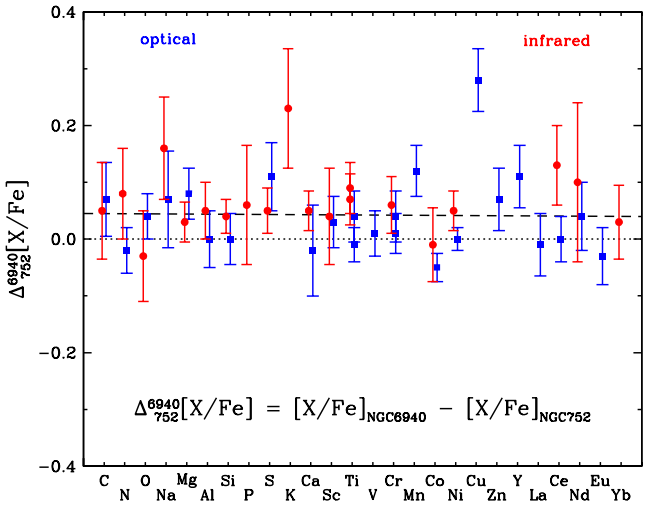

Figure 8. Differences between relative abundances [X/Fe] in NGC 752 and NGC 6940 in the optical and *IR* spectral regions. The dotted line at Δ^{6940}_{752}[X/Fe] = 0.00 indicates equality between [X/Fe] values in the two clusters. The dashed line at Δ^{6940}_{752}[X/Fe] = 0.04 represents the mean value for all abundances, excluding the aberrant values for K I in the *IR* and Cu I in the optical spectral region.

resolution ($R \simeq 60{,}000$) and high $S/N \geq 100$. The *H* and *K* band spectra for the two clusters were gathered with IGRINS set up as described in §3 and observed in identical fashions.

Our derived metallicities for the two clusters suggest that NGC 752 is slightly more metal-rich than NGC 6940. Defining Δ^{6940}_{752}X = X$_{\rm NGC6940}$ − X$_{\rm NGC752}$, from optical data Δ^{6940}_{752}[Fe I/H]$_{\rm opt}$ = +0.05 and Δ^{6940}_{752}[Fe II/H]$_{\rm opt}$ = +0.08, but these differences are well within the observational/analytical uncertainties. The *IR* metallicities are essentially identical: Δ^{6940}_{752}[Fe I/H]$_{\rm IR}$ = +0.02. We conclude, in agreement with past studies, that both NGC 6940 and NGC 752 have solar metallicities.

The general accord between the two clusters extends to the abundance ratios of individual elements. In Figure 8 we show abundance differences for all species studied in the optical and *IR* regions. The uncertainties shown in the figure are approximate, being averages of the σ values of the abundances in each cluster. Excluding the aberrant points for optical Cu I and *IR* K I, we derive $<\Delta^{6940}_{752}$[X/Fe]$>$ = +0.045 (+0.06 in the optical, +0.03 in the *IR*). The Cu difference is not well determined, as the NGC 752 optical spectra permitted use of only one Cu I feature. At present we lack an explanation for the 0.2 dex abundance difference between the *IR*-based K I lines in NGC 6940 and NGC 752. This issue will be considered again in our future studies of M67 and other OCs. In Ta-

Table 8. Abundance differences.

Species	N6940-N752	Lum - us	Carrera-us	Reddy-us
		Optical Spectral Region		
C	0.07	0.09		
N	−0.02	−0.20		
O	0.04	-0.02		
Na I	0.07	-0.07	−0.23	−0.08
Mg I	0.08	0.06	−0.03	0.00
Al I	0.00	0.36	−0.02	0.19
Si I	0.00	−0.11	−0.28	−0.11
S I	0.11			
K I				
Ca I	−0.02	−0.08	−0.15	−0.10
Sc II	0.03	−0.09		−0.09
Ti I	−0.01	0.11		−0.02
Ti II	0.04	−0.03		−0.11
V I	0.01	0.18		0.08
Cr I	0.01	0.00	−0.03	−0.08
Cr II	0.04	−0.30		−0.22
Mn I	0.12	0.24	0.17	0.07
Co I	−0.05	0.18		0.04
Ni I	0.00	−0.09	−0.12	−0.10
Cu I	0.28			0.16
Zn I	0.07	−0.08		−0.12
Y II	0.11	0.04		0.02
La II	−0.01			−0.09
Ce II	0.00	−0.04		0.02
Nd II	0.04	−0.07		−0.16
Eu II	−0.03			−0.09
average	0.04	0.00	−0.09	−0.04
sigma	0.07	0.15	0.14	0.10
		IGRINS H & K Spectral Region		
C	0.05	0.11		
N	0.08	−0.16		
O	−0.03	−0.17		
Na I	0.16	0.01	−0.15	0.00
Mg I	0.03	0.06	−0.03	0.00
Al I	0.05	0.30	−0.08	0.13
Si I	0.04	0.00	−0.17	0.00
P I	0.06			
S I	0.05			
K I	0.23			
Ca I	0.05	−0.05	−0.12	−0.07
Sc I	0.04			0.11
Ti I	0.07	0.12		−0.01
Ti II	0.09	0.18		0.10
Cr I	0.06	0.10	0.07	0.02
Co I	−0.01	0.10		−0.04
Ni I	0.05	−0.01	−0.04	−0.02
Ce II	0.13	−0.04		0.02
Nd II	0.10	−0.09		−0.18
Yb II	0.03			
average	0.07	0.03	−0.07	0.00
sigma	0.06	0.13	0.08	0.08

ble 8, we have listed the abundance differences between two clusters that generate Figure 8. Table 8 also contains the comparison with the recent optical abundances from the literature. The comparison with three studies (Carrera & Pancino 2011; Reddy et al. 2012; Lum & Boesgaard 2019) shows a general accord in uncertainty limits in both regions.

7 THE AGE OF NGC 752

In Paper I stellar evolutionary models with a solar abundance set were fitted to the CMD of NGC 6940, yielding an age of 1.15 Gyr. To well within the uncertainties, the metallicity that we have determined for NGC 752 is the same as that of NGC 6940. Both clusters appear to have the same helium abundance as well, given that (as discussed below) models for $Y = 0.270$ provide equally good fits to the luminosities of the core He-burning red clump (RC) stars if (a) distance moduli based on *Gaia* parallaxes are adopted, and (b) the observed RGs in the clusters are mostly in the RC evolutionary stage. Inspection of the CMD for NGC 6940 (Figure 1 of Paper 1) suggests that most RGs in that cluster are not associated with the RGB evolutionary tracks, and thus truly are RC stars. For NGC 752 we discuss this issue below, but for the moment simply assume that our program stars are mostly RCs. Then to derive our best estimate of the age of NGC 752, it is simply a matter of interpolating in the same model grids that were used in Paper I to identify which isochrone provides the best fit to the cluster turnoff stars.[2]

However, this process involves the cluster reddening, for which most estimates fall in the range $0.03 \leq E(B-V) \leq 0.05$ (Daniel et al. 1994; Taylor 2007; Schlafly & Finkbeiner 2011; Twarog et al. 2015), and the adopted color–$T_{\rm eff}$ relations (from Casagrande & VandenBerg 2018; hereafter CV18). Fortunately, the Sun provides a valuable constraint on both the predicted $T_{\rm eff}$ and color scales. According to CV18, their determinations of $M_{G,\odot} = 4.67$ and $(G - G_{\rm RP})_\odot = 0.49$ from reference solar spectra are accurate to within $\approx$ 0.01 mag. Encouragingly, the bolometric corrections (BCs) derived from the MARCS library of theoretical stellar fluxes (Gustafsson et al. 2008), yield the same value of M_G on the assumption of [Fe/H] = 0.0 and the solar values of $T_{\rm eff}$ and $\log g$, but a bluer $G - G_{\rm RP}$ color by $\approx$ 0.01 mag. We have therefore applied a +0.01 mag zero-point correction to the synthetic colors in order that our solar model reproduces the "observed" $G - G_{\rm RP}$ color of the Sun.

In Figure 9 we show the best model fits to the observed $(G - G_{RP}, G)$ color-magnitude diagram for NGC 752. The upper MS and turnoff stars are fit quite well by a 1.52 Gyr isochrone for solar abundances if the the adopted reddening is $E(B-V) = 0.035$ mag. The isochrone begins to deviate slightly to the blue of the observed MS at $G \sim 14$, with the offset in color at a given magnitude rising to as much as 0.1 mag at $G \sim 18$. Inadequacies in the CV18 color–$T_{\rm eff}$ relations for cooler stars are likely responsible for this problem given that the transmission function of the G filter extends well into the ultraviolet.

The tables of BCs presented by CV18 take into account the dependence of the extinction on spectral type in a fully consistent way; i.e., these transformations enable one to convert predicted luminosities and temperatures directly to absolute G and G_{RP} magnitudes that have been suitably corrected for an assumed reddening. In order for the resultant models to appear on the observed $(G - G_{RP}, G)$ CMD, they must then be shifted in the vertical direction by an amount corresponding to the true distance modulus, $(m - M)_0$. In Figure 9 the solar symbol indicates where the Sun would be located if it was as distant as NGC 752 and subject to the same reddening. The red filled circle represents a model at an age of 1.52 Gyr along an evolutionary track that has been calculated for a Standard Solar Model, and similarly adjusted by the adopted reddening and

[2] See Paper I for a fairly detailed description of the evolutionary codes and stellar models that are used in the present series of papers — including, in particular, a discussion of the treatment of convective core overshooting during the main-sequence (MS) phase.

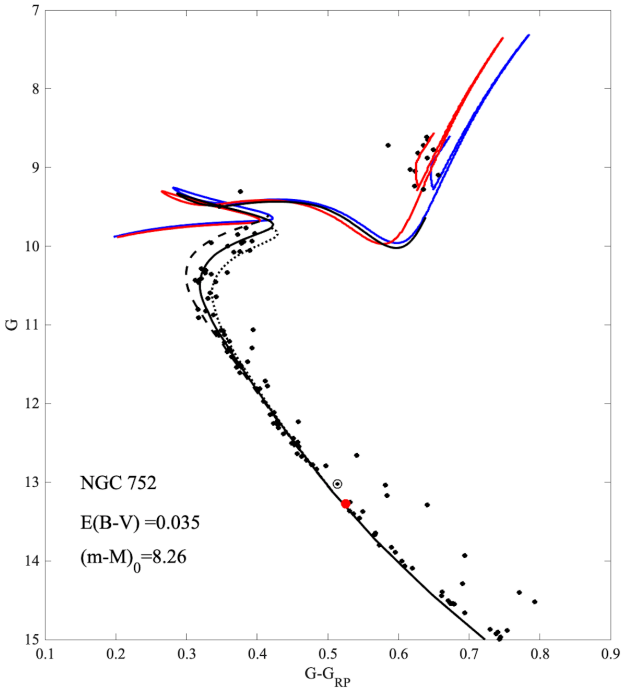

[t]

Figure 9. The CMD of NGC 752 (black dots) and its fit with a new 1.52 Gyr isochrone (solid black curve; dotted and dashed curves show 1.62 Gyr and 1.42 Gyr isochrones). The blue and red curves are the MESA evolutionary tracks computed for $M = 1.82\,M_{\odot}$, [Fe/H] = 0, $Y = 0.27$, assuming that $f_{\rm ov} = 0.035$ in Equation 1 from Paper I. The red track has the mixing length increased by 10% compared to the solar-calibrated value of $\alpha_{\rm MLT} = 2$ adopted for the blue track. See the text for descriptions of the solar symbol and the red dot.

distance modulus. Thus, in order to satisfy the solar constraint, the reddening of NGC 752 must be quite close to $E(B-V) = 0.035$ mag if it has $(m-M)_0 = 8.26$. The inferred reddening would be larger than this if the cluster is less distant, and vice versa.

Ages in the range of 1.7–2.0 Gyr were typically found for NGC 752 in the mid-1990s (e.g. Daniel et al. 1994; Dinescu et al. 1995), but subsequent determinations have generally favored ages closer to 1.5 Gyr (e.g. Anthony-Twarog & Twarog 2006; Twarog et al. 2015). The earlier age determinations are especially uncertain because the stellar models used in those studies assumed little or no overshooting from convective cores during the MS phase. Because such isochrones are incapable of reproducing the observed turnoff morphology, the ages derived from them are highly questionable. In contrast, later investigations employed models that allowed for significant amounts of core overshooting, resulting in fits to the NGC 752 CMD that are quite similar to that shown in Fig. 9, and they yield ages that have little ambiguity.

Recently, a similar color-magnitude diagram study by Agüeros et al. (2018) obtained an age of 1.34 ± 0.06 Gyr for NGC 752, which is inconsistent with our determination by more than $2\,\sigma$. Although those researchers used a sophisticated Bayesian approach to determine the cluster parameters (including such observational properties as the distance, metallicity, and extinction) from fits of isochrones to the photometric data, their results will be subject to systematic errors that are very difficult to quantify. In particular, the predicted $T_{\rm eff}$ scale is quite sensitive to, e.g., the adopted atmospheric boundary condition and the treatment of super-adiabatic convection. Errors in the adopted color transformations can further impact how well stellar models are able to reproduce an observed CMD. Consequently, one cannot rely on such isochrone predictions as the location of the giant branch relative to the turnoff to provide a useful constraint on absolute cluster ages (see, e.g., Vandenberg et al. (1990), who show that this diagnostic may be used to obtain accurate *relative* ages of star clusters.) We suspect that the derivation by Agüeros et al. of $A_V = 0.198 \pm 0.0085$ mag, which is appreciably higher than most determinations, including the line-of-sight Galactic extinction (Schlafly & Finkbeiner 2011), can be attributed, in part, to errors in the model $T_{\rm eff}$ and/or color scales.

Isochrones appropriate to young and intermediate-age clusters are also very dependent on how much overshooting from convective cores during the MS phase is assumed. In fact, the MESA models (Choi et al. 2016) that were used by Agüeros et al. assume a value of the overshooting parameter that is, according to our analysis (see Paper I and the next section) too low by about a factor of two. This appears to be the main reason (see below) why they obtained a significantly younger age than our determination. Unfortunately, Agüeros et al. do not include a figure that compares their best-fit isochrone with the CMD of NGC 752; hence it is not possible to make a visual assessment of how well the data are fitted. Our age determination should be particularly robust because we have used the Sun to calibrate the predicted $T_{\rm eff}$ and color scales, and have adopted the *Gaia* distance and a spectroscopically derived metallicity, from which we have deduced the $E(B-V) \approx 0.035$ in order to achieve consistency with the solar constraint. Thus, nearly all of the cluster parameters are derived independently of our stellar models and the age is effectively obtained from an overlay of the isochrone that provides the best fit to the turnoff stars.

8 STELLAR EVOLUTION MODELING OF NGC 752

In Paper I we emphasized the importance of calibrating the efficiency of convective overshooting beyond the Schwarzschild boundary of the hydrogen convective core in MS stars with $1 \lesssim M/M_{\odot} \lesssim 2$. In the Victoria stellar evolution code employed here to generate isochrones, the convective overshooting is estimated using the integral equations of Roxburgh (1989) as described in VandenBerg et al. (2006). In particular, Figure 1 in the latter paper shows the variation of the free parameter $F_{\rm over}$ in Roxburgh's equations calibrated by comparing the predicted and observed CMDs for a number of open clusters with different ages. This parameter starts to increase from $F_{\rm over} = 0$ at $M \approx 1.14\,M_{\odot}$, reaches a maximum value of $F_{\rm over} = 0.55$ at $M = 1.7\,M_{\odot}$ and then remains constant. In the MESA code, that we use to model the evolution of MS turn-off (MSTO) stars up to the red-clump (RC) phase, the convective overshooting is approximated by a diffusion coefficient that is exponentially decreasing outside the convective boundary on a lengthscale of $0.5 f_{\rm ov} H_P$, where H_P is a local pressure scale height. In Paper I we showed that the MESA code with $f_{\rm ov} = 0.035$ produces a stellar evolution track for an initial mass $M = 2\,M_{\odot}$ that is approximately equal to the MSTO mass of stars in the open cluster NGC 6940, in the excellent agreement with the Victoria 1.15 Gyr isochrone generated for this cluster.

The MSTO mass for the estimated 1.52 Gyr age of NGC 752 is $M \approx 1.8\,M_{\odot}$. This mass is high enough that the maximum value of $F_{\rm over} = 0.55$ should still be used according to Figure 1 in VandenBerg et al. (2006). Therefore we have used the same value of $f_{\rm ov} = 0.035$ in the MESA code to model the evolution of MSTO stars in NGC 752. Figure 9 demonstrates that in this case the evolu-

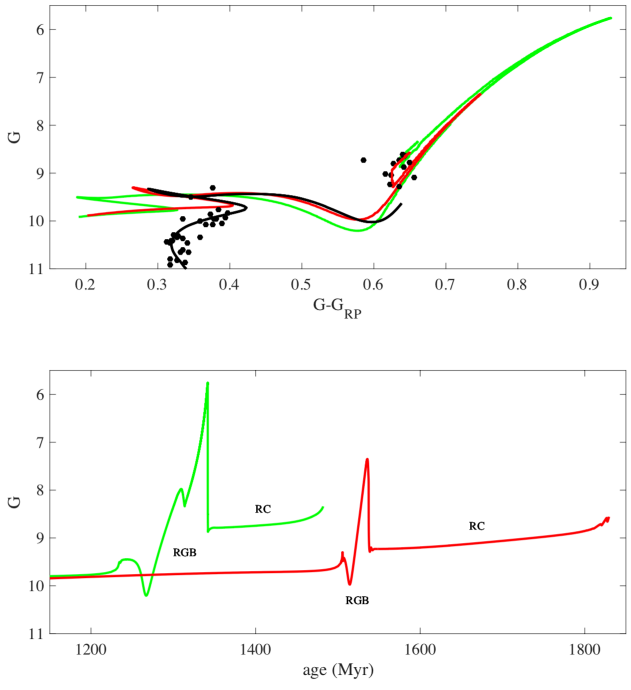

[t]

Figure 10. Upper panel: the MESA evolutionary tracks of the solar-metallicity 1.82 $M_\odot$ model with the convective overshooting parameter f_{ov} = 0.035 (red) and of the 1.85 $M_\odot$ model with f_{ov} = 0.016 (green) that both fit the luminosity of the stars leaving the MS in NGC 752. Lower panel: the RGB and RC evolutionary timescales of these models.

tionary track for the initial mass 1.82 $M_\odot$ (blue curve) is again in an excellent agreement with a post-MSTO part of the isochrone (black curve).

We believe that most/all of our program stars are red clump (RC) members. First, their derived CNO abundances and $^{12}C/^{13}C$ ratios are all consistent with evolution beyond the first-ascent RGB, with completion of "first dredge-up" envelope mixing of CN-cyle products. Second, stars with the NGC 752 turnoff mass should spend little time on the upper RGB, and none are observed. Based on the comparison of the timescales of the RGB and RC evolution for our best-fit stellar model, we conclude that most of the red giants observed in NGC752 should be RC stars.

As in Paper I, the red giant branches of the track and the isochrone are ~ 0.05 mag redder than they should be for the track to be able to almost perfectly fit the colors of the RC stars in NGC 752 on the following He-core burning evolutionary phase. Possible causes of this small discrepancy are mentioned in Paper I. To show that our track can successfully reproduce colors and magnitudes of RC stars in NGC 752, we have increased the solar-calibrated convective mixing length parameter α_{MLT} = 2.0 used for the red track by 10%. This has enhanced heat transport in the convective envelopes of our RGB and RC model stars and, as a result, changed their colors by ~ −0.05 (red curve in Figure 9). We used the same remedy in Paper I. It does not solve the problem of the RGB color discrepancy, but it enables us to see how the RGB and RC evolutionary tracks will look after the true cause of this discrepancy is found and fixed.

When we reduce the convective overshooting parameter in our solar-metallicity 1.82 $M_\odot$ MESA stellar models to f_{ov} = 0.016 (the value used by Choi et al. 2016 for core overshooting), and slightly increase the initial mass to 1.85 $M_\odot$ to keep the same MSTO luminosity, the morphology of their corresponding evolutionary track becomes inconsistent with the observed CMD of NGC 752 (green curves in Figure 10). There are multiple problems: (a) the effective temperature at the end of the core H-burning phase is too high; (b) the track produced by core He-burning is too narrow in color and it does not reach the minimum luminosity of the observed RC stars (top panel); and (c) the RGB and RC evolutionary timescales are now comparable (bottom panel), which would lead us to expect comparable numbers of RGB and RC stars in NGC 752, which is not observed. The last inconsistency arises because the reduced efficiency of convective H-core overshooting leads to an extended RGB evolution with the He core becoming electron degenerate and experiencing a flash at the end, while in the models with f_{ov} = 0.035 the He core remains non-degenerate, and He in the core is ignited quiescently.

Applying these evolutionary computations to C and N abundances, in the upper panel of Figure 11 we compare the predicted and observed [C/Fe] abundance ratios for the RC stars in NGC 752. The observed C abundances can be reproduced by our models only if we assume that they were already slightly reduced initially by ≃ 0.1 dex, compared to the solar-scaled [C/Fe] ratio (the dashed black curve), because without this assumption the predicted RC abundance is [C/Fe] = −0.19. while our mean observed value is [C/Fe] = −0.31 ± 0.06. Lum & Boesgaard (2019) support a slightly subsolar initial C abundance in NGC 752, deriving [C/Fe] = −0.10 (σ =0.13, 21 stars). However, the Lum & Boesgaard red giant abundance, [C/Fe] = −0.22 (σ =0.08, 6 stars) is consistent with our predictions with solar or slightly subsolar initial C abundances.

In the lower panel of Figure 11 we make the same kind of comparison for N. The observed optical and *IR* values, [N/Fe] = 0.48 ± 0.02 and 0.44 ± 0.08, respectively, are slightly larger than the predictions, [N/Fe] = 0.41 (red curve) and 0.37 (black dashed curve) The initial N abundance has been assumed to be solar. However, Lum & Boesgaard (2019) derives [N/Fe] = 0.12 (no stated σ), and that would raise the predicted red giant N abundance to be nearly comparable to the observed one.[3]

Finally, for carbon isotopic ratios our model predicts $^{12}C/^{13}C$ = 22.2 and 20.9 for the red and black dashed tracks. They are comparable with the mean C isotopic ratios measured in the RC stars in NGC 752: $^{12}C/^{13}C$= 22 (optical) and 16 (*IR*). Note that our predicted C and N abundances are in a good agreement with those obtained for a non-rotating 1.8 $M_\odot$ star by Charbonnel & Lagarde (2010) ($^{12}C/^{13}C$ = 19.9, [C/Fe] = −0.18, [N/Fe] = 0.37), who did not consider any convective overshooting, but did include thermohaline mixing on the RGB. In our models, the enhanced convective overshooting significantly decreases the RGB evolution time (the lower panel in Figure 10), therefore if we included thermohaline mixing on the RGB its effect on the surface abundances of C and N would be even less pronounced and our assumption on the reduced initial abundance of C would still be required. According to Charbonnel & Lagarde (2010), rotation with a ZAMS velocity of 110 km s^{-1} only slightly changes these abundances to $^{12}C/^{13}C$ = 15.2, [C/Fe] = −0.19 and [N/Fe] = 0.31.

[3] The Lum & Boesgaard (2019) red giant abundance mean is [N/Fe] = 0.28 (σ = 0.07), somewhat lower than our predicted and observed N values.

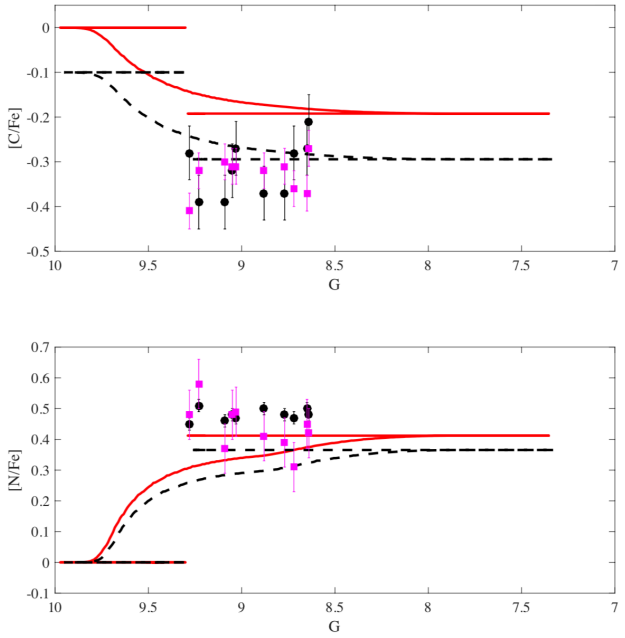

Figure 11. The predicted changes of the surface C (top panel) and N (bottom panel) abundances for the solar-metallicity 1.82 $M_{\odot}$ stellar evolutionary tracks computed with f_{ov} = 0.035 and α_{MLT} = 2.2 are compared with the C and N abundances determined for the red-clump stars in NGC 752 using optical (black circles) and infrared (magenta squares) spectra. The red and black dashed curves are obtained assuming that the initial C abundance is [C/Fe] = 0 and [C/Fe] = −0.1, respectively.

9 SUMMARY

This is the second of three papers that report analyses of high-resolution optical and *IR* spectra RG members of prominent OCs. In this study, we have performed the detailed chemical abundance analysis for 10 RGs in the NGC 752 open cluster using the high-resolution near-*IR* *H* and *K* band spectral data obtained with the IGRINS spectrograph. BT15 investigated the same RG members in the optical region from their high-resolution optical spectra, and here we combine data from both regions and explore the NGC 752 from a more complete wavelength window.

We revisited the CMD of NGC 752, investigating the membership assignments using *Gaia* DR2 (Gaia Collaboration et al. 2018). We applied a Gaussian mixture model to set the parallax bounds, leading to an estimated cluster distance of 448 pc with a true distance modulus of $(m - M)_0$ = 8.26. We also remeasured the radial velocities of our targets from the *H* and *K* band spectra, finding a cluster mean of 4.97 ± 0.24 km s^{-1} (Table 1), which is in general agreement with both our previous optical RV (Paper 1) and *Gaia*.

We applied LDR relations reported by Fukue et al. (2015) and estimated the *IR*-LDR effective temperatures for our targets. LDR temperatures obtained from both optical and *IR* line depth ratios are in good agreement with the spectral temperatures within ∼150 K, indicating that this method provides reliable temperature estimations in the cases of lack of information from the optical region. This encouraging result paves the way for dust-obscured open cluster chemical composition studies.

Adopting the model atmospheric parameters from Paper 1, we performed detailed abundance analysis for 20 elements in the *H* and *K* band spectral regions of our targets. The abundances for 18 of these elements were determined both in the optical and *IR* regions. In general, we derived the abundances of H-burning, α, light odd-Z, Fe-group, and *n*-capture elements, and also determined $^{12}C/^{13}C$ ratios from both regions. In general, they are in accord with their optical counterparts and have abundances similar to their solar-system values. *IR* abundances of CNO and some α elements (such as Mg and S) were found to be more reliable compare to their optical counterparts due to more number of lines and regions used during the *IR* spectral analysis.

In some cases, small abundance differences were seen between neutral and ionized species of the same element. In particular there is only one Ti II line present in the *H* band and, compare to its optical counterparts, it seems to yield sub-solar abundances for our stars in general. Further investigation is needed to better understand this issue. For Sc abundances, Sc II and Sc I lines were used in the optical and *IR* regions, respectively. Their mean Sc cluster abundance differs by 0.12 dex. But only two weak Sc I lines in the *K* band with hyperfine structures were used to determine the *IR* Sc abundances, so we do not regard this as a significant discrepancy.

To the best of our knowledge, P, S and K abundances have been derived here for the first time for our targets, and all are consistent with solar abundances in NGC 752. Potassium abundances obtained from two lines in the *H* band indicate that these lines are likely to be less affected by non-LTE line formation problems than is the strong K I 7698.7 Å resonance line. A similar suggestion could be made for the *IR* Na lines. They provide Na abundances ∼0.1 dex lower than the optical ones, which might indicate that they are also less affected by non-LTE conditions.

Five *n*-capture elements were identified in the spectra of NGC 752 RGs. The *n*-capture abundances in our stars resulted in somewhat overabundances both in the *s*-process and *r*-process elements, later being less slightly overabundant. Encouragingly, the abundances of Ce and Nd, show agreement between their optical and *IR* values. Detection of a Yb II line at 16498.4 Å in the *H* band provides a unique opportunity to study this element, since the strong resonance Yb II 3694 Å line occurs in a very crowded low-flux region of cool stars, essentially useless for abundance studies in most solar-metallicity stars.

Analyzing CNO abundances using the many available *IR* CO, CN, and OH molecular features, we found cluster mean abundances from optical and *IR* regions to be in reasonable agreement. We suggest that *IR* O abundances may provide more robust O abundances than does the [O I] 6300.3 Å optical line. Our study multiple ^{12}CO and ^{13}CO first overtone band lines yields a similar endorsement: these regions provide more robust measurements of $^{12}C/^{13}C$ values than ones possible from the weak CN optical features near 8004 Å. Our CNO results indicate that all NGC 752 RC stars have abundances consistent with those predicted from first dredge-up predictions, e.g., Charbonnel & Lagarde (2010).

We used the NGC 752 CMD to investigate the evolutionary states of 10 RG members, first concluding that they are at least mostly red clump members. The best evolutionary model for solar metallicity yielded core He-burning RC stars consistent with our stars if a helium abundance Y = 0.270 is adopted. Isochrones fitted to the cluster turnoff yield an age of 1.52 Gyr for the reddening $E(B - V)$ = 0.035 mag and the turnoff mass M = 1.82 $M_{\odot}$ of NGC 752. Our light element abundance values, $\langle$[C/Fe]$\rangle \simeq -0.32$, $\langle$[N/Fe]$\rangle \simeq +0.46$, $\langle$[C/Fe]$\rangle \simeq -0.05$, and $\langle^{12}C/^{13}C\rangle \simeq 22$, are in reasonable accord with those predicted by our MESA evolutionary models.

ACKNOWLEDGMENTS

This study has been supported by the US National Science Foundation (NSF, grant AST 16-16040), and by the University of Texas Rex G. Baker, Jr. Centennial Research Endowment. This work used the Immersion Grating Infrared Spectrometer (IGRINS) that was developed under a collaboration between the University of Texas at Austin and the Korea Astronomy and Space Science Institute (KASI) with the financial support of the US National Science Foundation under grant AST-1229522, of the University of Texas at Austin, and of the Korean GMT Project of KASI. These results made use of spectra obtained at the Discovery Channel Telescope at Lowell Observatory, and the 2.7m Smith telescope at McDonald Observatory. Lowell is a private, non-profit institution dedicated to astrophysical research and public appreciation of astronomy and operates the DCT in partnership with Boston University, the University of Maryland, the University of Toledo, Northern Arizona University and Yale University. We also gathered data from the European Space Agency (ESA) mission *Gaia* (https : //www.cosmos.esa.int/gaia), processed by the *Gaia* Data Processing and Analysis Consortium (DPAC, https : //www.cosmos.esa.int/web/gaia/dpac/consortium). Funding for the DPAC has been provided by national institutions, in particular the institutions participating in the *Gaia* Multilateral Agreement. This research has made use of NASA's Astrophysics Data System Bibliographic Services; the SIMBAD database and the VizieR service, both operated at CDS, Strasbourg, France. This research has made use of the WEBDA database, operated at the Department of Theoretical Physics and Astrophysics of the Masaryk University, and the VALD database, operated at Uppsala University, the Institute of Astronomy RAS in Moscow, and the University of Vienna.

10 APPENDIX

The Gaussian mixture model is of the form:

$$\Phi(\mu_{x_i}, \mu_{y_i}, \epsilon_{x_i}, \epsilon_{y_i}) = \phi_c + \phi_f \tag{2}$$

where

$$\phi_c = \frac{1 - N_f}{2\pi\sqrt{\sigma_{c,x}^2 + \epsilon_{x_i}^2}\sqrt{\sigma_{c,y}^2 + \epsilon_{y_i}^2}\sqrt{1-\rho_c^2}} exp[-\frac{\alpha}{2(1-\rho_c^2)}] \tag{3}$$

$$\tag{4}$$

$$\phi_f = \frac{N_f}{2\pi\sqrt{\sigma_{f,x}^2 + \epsilon_{x_i}^2}\sqrt{\sigma_{f,y}^2 + \epsilon_{y_i}^2}\sqrt{1-\rho_f^2}} exp[-\frac{\beta}{2(1-\rho_f^2)}] \tag{5}$$

$$\tag{6}$$

and where

$$\alpha = \frac{(\mu_{x_i} - \mu_{c,x})^2}{\sigma_{c,x}^2 + \epsilon_{x_i}^2} - \frac{2\rho_c(\mu_{x_i} - \mu_{c,x})(\mu_{y_i} - \mu_{c,y})}{\sqrt{\sigma_{c,x}^2 + \epsilon_{x_i}^2}\sqrt{\sigma_{c,y}^2 + \epsilon_{y_i}^2}} + \frac{(\mu_{y_i} - \mu_{c,y})^2}{\sigma_{c,y}^2 + \epsilon_{y_i}^2} \tag{7}$$

$$\beta = \frac{(\mu_{x_i} - \mu_{f,x})^2}{\sigma_{f,x}^2 + \epsilon_{x_i}^2} - \frac{2\rho_f(\mu_{x_i} - \mu_{f,x})(\mu_{y_i} - \mu_{f,y})}{\sqrt{\sigma_{f,x}^2 + \epsilon_{x_i}^2}\sqrt{\sigma_{f,y}^2 + \epsilon_{y_i}^2}} + \frac{(\mu_{y_i} - \mu_{f,y})^2}{\sigma_{f,y}^2 + \epsilon_{y_i}^2} \tag{8}$$

The notation for the *Gaia* DR2 proper motion data and the 11 model parameters is as follows:

μ_{x_i}, μ_{y_i} = proper motion components for i^{th} star
$\epsilon_{x_i}, \epsilon_{y_i}$ = proper motion component errors for i^{th} star
N_f = field scaling parameter
$\mu_{c,x}, \mu_{c,y}$ = cluster center
$\mu_{f,x}, \mu_{f,y}$ = field center
$\sigma_{c,x}, \sigma_{c,y}$ = cluster std. deviations
$\sigma_{f,x}, \sigma_{f,y}$ = field std. deviations
ρ_c, ρ_f = cluster and field correlation coefficients

While it is common to use ordinary maximum likelihood estimation to determine the parameters defining mixture models, as Sanders (1971) did, we used an expectation-maximization (EM) machine-learning algorithm for finite mixtures as derived by Dempster et al. (1977). We found that convergence of the model parameters using EM was more reliable than when applying MLE to our model. Central to the EM algorithm, the expectation of our complete-data log-likelihood function is of the form

$$Q = \sum_{i=1}^{NST} T_{c_i} \log(\phi_{c_i}) + T_{f_i} \log(\phi_{f_i}), \tag{9}$$

where NST is the number of total stars in our data set, and ϕ_{c_i} and ϕ_{f_i} are simply ϕ_c and ϕ_f evaluated at the i^{th} star using the current parameter guesses. T_{c_i} and T_{f_i} are the conditional probabilities that the i^{th} star belongs to the cluster or field distribution, respectively. They are calculated with $T_{c_i} = \phi_{c_i}/(\phi_{c_i} + \phi_{f_i})$ and $T_{f_i} = \phi_{f_i}/(\phi_{c_i} + \phi_{f_i})$. In our EM algorithm, 9 was maximized with respect to each of the 11 parameters numerically and the probabilities, which feed into it, were in turn updated. This process was iterated until convergence of the parameters. While the conditional probabilities T_{c_i} and T_{f_i} changed during the process of running the EM algorithm, the final T_{c_i} probabilities after parameter convergence were the probabilities that we used for cluster membership determination.

REFERENCES

Afşar M., et al., 2018, ApJ, 865, 44
Agüeros M. A., et al., 2018, ApJ, 862, 33
Anthony-Twarog B. J., Twarog B. A., 2006, PASP, 118, 358
Arenou F., et al., 2018, A&A, 616, A17
Asplund M., Grevesse N., Sauval A. J., Scott P., 2009, ARA&A, 47, 481
Biazzo K., Frasca A., Catalano S., Marilli E., 2007a, Astronomische Nachrichten, 328, 938
Biazzo K., et al., 2007b, A&A, 475, 981
Böcek Topcu G., Afşar M., Schaeuble M., Sneden C., 2015, MNRAS, 446, 3562
Böcek Topcu G., Afşar M., Sneden C., 2016, MNRAS, 463, 580
Böcek Topcu G., et al., 2019, MNRAS, 485, 4625
Brogaard K., et al., 2012, A&A, 543, A106
Cantat-Gaudin T., et al., 2018, A&A, 618, A93
Carrera R., Pancino E., 2011, A&A, 535, A30
Casagrande L., VandenBerg D. A., 2018, MNRAS, 479, L102
Charbonnel C., Lagarde N., 2010, A&A, 522, A10
Choi J., Dotter A., Conroy C., Cantiello M., Paxton B., Johnson B. D., 2016, ApJ, 823, 102
Cutri R. M., et al., 2003, VizieR Online Data Catalog, 2246, 0
Daniel S. A., Latham D. W., Mathieu R. D., Twarog B. A., 1994, PASP, 106, 281 (Dan94)
Dempster A. P., Laird N. M., Rubin D. B., 1977, J. Roy. Stat. Soc., Ser. B, 39, 1

Dinescu D. I., Demarque P., Guenther D. B., Pinsonneault M. H., 1995, AJ, 109, 2090
Fukue K., et al., 2015, ApJ, 812, 64
Gaia Collaboration et al., 2016, A&A, 595, A1
Gaia Collaboration et al., 2018, A&A, 616, A1
Gray D. F., Johanson H. L., 1991, PASP, 103, 439
Gully-Santiago M., Wang W., Deen C., Jaffe D., 2012, in Modern Technologies in Space- and Ground-based Telescopes and Instrumentation II. p. 84502S, doi:10.1117/12.926434
Gustafsson B., Edvardsson B., Eriksson K., Jørgensen U. G., Nordlund Å., Plez B., 2008, A&A, 486, 951
Kovtyukh V. V., Soubiran C., Bienaymé O., Mishenina T. V., Belik S. I., 2006, MNRAS, 371, 879
Lawler J. E., Hala Sneden C., Nave G., Wood M. P., Cowan J. J., 2019, ApJS, 241, 21
Lee J.-J., Gullikson K., Kaplan K., 2017, igrins/plp 2.2.0, doi:10.5281/zenodo.845059, https://doi.org/10.5281/zenodo.845059
Lum M. G., Boesgaard A. M., 2019, ApJ, 878, 99
Mace G., et al., 2016, in Ground-based and Airborne Instrumentation for Astronomy VI. p. 99080C, doi:10.1117/12.2232780
Mace G., et al., 2018, in Ground-based and Airborne Instrumentation for Astronomy VII. p. 107020Q, doi:10.1117/12.2312345
Mermilliod J. C., Mayor M., Udry S., 2008, A&A, 485, 303
Mucciarelli A., Merle T., Bellazzini M., 2017, A&A, 600, A104
Park C., et al., 2014, in Ground-based and Airborne Instrumentation for Astronomy V. p. 91471D, doi:10.1117/12.2056431
Pilachowski C. A., Hobbs L. M., 1988, PASP, 100, 336
Pilachowski C. A., Pace C., 2015, AJ, 150, 66
Reddy A. B. S., Giridhar S., Lambert D. L., 2012, MNRAS, 419, 1350
Roxburgh I. W., 1989, A&A, 211, 361
Salaris M., Weiss A., Percival S. M., 2004, A&A, 414, 163
Sanders W. L., 1971, A&A, 14, 226
Schlafly E. F., Finkbeiner D. P., 2011, ApJ, 737, 103
Takeda Y., Zhao G., Chen Y.-Q., Qiu H.-M., Takada-Hidai M., 2002, PASJ, 54, 275
Takeda Y., Omiya M., Harakawa H., Sato B., 2016, PASJ, 68, 81
Taylor B. J., 2007, AJ, 134, 934
Thorsbro B., Ryde N., Schultheis M., Hartman H., Rich R. M., Lomaeva M., Origlia L., Jönsson H., 2018, ApJ, 866, 52
Tull R. G., 1998, in D'Odorico S., ed., Proc. SPIE Vol. 3355, Optical Astronomical Instrumentation. pp 387–398, doi:10.1117/12.316774
Tull R. G., MacQueen P. J., Sneden C., Lambert D. L., 1995, PASP, 107, 251
Twarog B. A., Anthony-Twarog B. J., Deliyannis C. P., Thomas D. T., 2015, AJ, 150, 134
VandenBerg D. A., Bergbusch P. A., Dowler P. D., 2006, ApJS, 162, 375
Vandenberg D. A., Bolte M., Stetson P. B., 1990, AJ, 100, 445
Yuk I.-S., et al., 2010, in Ground-based and Airborne Instrumentation for Astronomy III. p. 77351M, doi:10.1117/12.856864
Zhao J. L., He Y. P., 1990, A&A, 237, 54

This paper has been typeset from a TEX/LATEX file prepared by the author.